

ACCEPTED MANUSCRIPT

A new front-tracking Lagrangian model for the modeling of dynamic and post-dynamic recrystallization

To cite this article before publication: Sebastian Florez *et al* 2021 *Modelling Simul. Mater. Sci. Eng.* in press <https://doi.org/10.1088/1361-651X/abd837>

Manuscript version: Accepted Manuscript

Accepted Manuscript is “the version of the article accepted for publication including all changes made as a result of the peer review process, and which may also include the addition to the article by IOP Publishing of a header, an article ID, a cover sheet and/or an ‘Accepted Manuscript’ watermark, but excluding any other editing, typesetting or other changes made by IOP Publishing and/or its licensors”

This Accepted Manuscript is © 2020 IOP Publishing Ltd.

During the embargo period (the 12 month period from the publication of the Version of Record of this article), the Accepted Manuscript is fully protected by copyright and cannot be reused or reposted elsewhere.

As the Version of Record of this article is going to be / has been published on a subscription basis, this Accepted Manuscript is available for reuse under a CC BY-NC-ND 3.0 licence after the 12 month embargo period.

After the embargo period, everyone is permitted to use copy and redistribute this article for non-commercial purposes only, provided that they adhere to all the terms of the licence <https://creativecommons.org/licenses/by-nc-nd/3.0>

Although reasonable endeavours have been taken to obtain all necessary permissions from third parties to include their copyrighted content within this article, their full citation and copyright line may not be present in this Accepted Manuscript version. Before using any content from this article, please refer to the Version of Record on IOPscience once published for full citation and copyright details, as permissions will likely be required. All third party content is fully copyright protected, unless specifically stated otherwise in the figure caption in the Version of Record.

View the [article online](#) for updates and enhancements.

A new front-tracking Lagrangian model for the modeling of dynamic and post-dynamic recrystallization

Sebastian Florez¹, Karen Alvarado¹, Marc Bernacki¹

¹ Mines-ParisTech, PSL-Research University, CEMEF – Centre de mise en forme des matériaux, CNRS UMR 7635, CS 10207 rue Claude Daunesse, 06904 Sophia Antipolis Cedex, France

E-mail: sebastian.florez@mines-paristech.fr

22 September 2020

Abstract.

A new method for the simulation of evolving multi-domains problems has been introduced in previous works (RealIMotion), Florez et al. (2020) and further developed in parallel in the context of isotropic Grain Growth (GG) with no consideration for the effects of the Stored Energy (SE) due to dislocations. The methodology consists in a new front-tracking approach where one of the originality is that not only interfaces between grains are discretized but their bulks are also meshed and topological changes of the domains are driven by selective local remeshing operations performed on the Finite Element (FE) mesh. In this article, further developments and studies of the model will be presented, mainly on the development of a model taking into account grain boundary migration by (GBM) SE. Further developments for the nucleation of new grains will be presented, allowing to model Dynamic Recrystallization (DRX) and Post-Dynamic Recrystallization (PDRX) phenomena. The accuracy and the performance of the numerical algorithms have been proven to be very promising in Florez et al. (2020). Here the results for multiple test cases will be given in order to validate the accuracy of the model taking into account GG and SE. The computational performance will be evaluated for the DRX and PDRX mechanisms and compared to a classical FE framework using a Level-Set (LS) formulation.

Submitted to: *Modelling Simul. Mater. Sci. Eng.*

1
2
3 *A new front-tracking Lagrangian model for the modeling of DRX and PDRX* 2

4 **1. Introduction**

5
6
7 The modeling, at the mesoscopic scale, of Grain Growth (GG) and recrystallization
8 (ReX) in polycrystalline materials during thermal and mechanical treatments has been
9 the focus of numerous studies in the last decades. Indeed, mechanical and functional
10 properties of metals are strongly related to their microstructures which are themselves
11 inherited from thermal and mechanical processing.
12
13

14
15 When looking to the so-called full-field (FF) methods, based on a full description
16 of the microstructure topology and modeling of grain boundary migration (GBM) at
17 mesoscopic scale, main numerical frameworks involve: Monte Carlo (MC) [1, 2], Cellular
18 Automata (CA) [3, 4, 5, 6], Multi Phase-Field (MPF) [7, 8, 9, 10], Vertex/Front-Tracking
19 [11, 12, 13, 14, 15] or Level-Set (LS) [16, 17, 18, 19] models. These numerical methods
20 are developed by many researchers [20]. All the mentioned methods have, of course,
21 their own strengths and weaknesses [20, 21].
22
23

24
25 When large deformation have to be considered (common in metal forming con-
26 text), LS or MPF approaches in context of unstructured Finite Element (FE) mesh and
27 FE remeshing strategies, remain the main powerful and generic approaches but with a
28 strong limitation in terms of computational cost.
29
30

31
32 In this context vertex and front tracking approaches appear as interesting candi-
33 dates. An explicit description of the interfaces is considered and GBM is imposed at
34 each increment by computing the velocity of the nodes describing the interfaces. While
35 having a deterministic resolution (solving of partial differential equation - PDE), this
36 methodology is very efficient. However, the implementation of algorithms allowing topo-
37 logical event in this context is not straightforward and the fact that these methods do
38 not describe the bulk of the grains could be limiting for some metallurgical mechanisms,
39 such as the appearance of new grains (nucleation is in general only taken into account
40 exclusively at the vicinity of multiple junctions) or substructures inside the grains.
41
42
43

44
45 Previous works [22, 23] have been dedicated to the creation of an improved
46 front-tracking method solving these weaknesses. The model denominated TOPological
47 REmeshing in lAgrangian framework for Large interface MOTION (ToRealMotion,
48 hereafter TRM) maintains the interior of grains meshed, handling with relative ease
49 the topological changes of the grain boundary network and allowing the treatment of
50 in-grain operations and at a higher computational performance than classical FE-LS
51 models for the same accuracy. The objective of the present article is then to extend and
52 apply the TRM model to handle DRX and PDRX phenomena, namely, reproducing
53 previous methodologies for the modeling of these mechanisms, published in a FE-LS
54 context [36].
55
56
57
58
59
60

1
2
3 *A new front-tracking Lagrangian model for the modeling of DRX and PDRX* 3

4
5 **2. The TRM model : Isotropic Grain Growth context**

6
7 The TRM model has been presented in a previous work in [22], then adapted to a parallel
8 computational environment in [23]. This model uses the logic behind front-tracking
9 methods where the discretization of interfaces is the minimal topological information
10 allowing to model 2D-GBM. The TRM model goes a step further by implementing also a
11 discretization of the interior of the grains in the form of simplexes to allow the interaction
12 of the grain boundaries with the bulk of the grains and preventing inconsistencies of
13 the physical domain such as the overlapping of regions. The data structure of the
14 TRM model is then built on top of a mesh with elements and nodes, enabling also the
15 possibility to compute FE problems on it (see section 2.1 of [22] for more information
16 regarding the data structure of the TRM model).
17
18

19
20 This data structure contains the pieces of information needed to describe discrete
21 geometrical entities such as *Points*, *Lines* and *Surfaces*. The classification of these
22 entities is helpful when computing geometric properties: the area of surfaces can be
23 computed by adding the contribution of each element of the grain, while the curvature
24 κ and normal \vec{n} of interfaces can be obtained by approximating the interface with a high
25 order mathematical form (higher than the linear discretization of the domain) such as
26 a least square approximation or with piece-wise polynomials such as natural parametric
27 splines. We have opted to use the latter in order to obtain such geometrical quantities.
28
29
30
31

32 The TRM model allows *physical* mechanisms to be simulated. These physical mech-
33 anisms represent how the different geometries are supposed to evolve and interact based
34 on their current state. The TRM model has been developed to move the different nodes
35 of the mesh based on a user-defined velocity field \vec{v} and a time step dt . Once a velocity
36 is defined a new position for each node N_i on the mesh can be obtained:
37
38
39

$$40 \quad \vec{u}_i^{t+dt} = \vec{u}_i + \vec{v}_i \cdot dt, \quad (1)$$

41
42 where \vec{u}_i is the current position of the node N_i and \vec{u}_i^{t+dt} is the position of node N_i
43 in the next increment.
44

45 Here, each node displacement can potentially produce an overlap ‡ of some of the
46 elements attached to the node. The TRM model hence ensures the local conformity
47 of the mesh employing a “locally-iteratively movement-halving”, that finds iteratively
48 the approximated maximal displacement that a node can make in the direction of the
49 velocity v_i before an overlap takes place. This procedure ensures at all times that both,
50 the mesh and the microstructural domain are valid.
51
52
53

54 Once several steps of Lagrangian movement are performed, it is highly probable
55 that the quality of the mesh become too poor to continue with the GBM, this is why
56

57 ‡ An overlap in a mesh is produced when an element is partially or completely superposed by another
58 element hence disrupting the 1:1 mapping of the numerical domain to the physical domain, such a mesh
59 can not be used in a Finite Element resolution.
60

A new front-tracking Lagrangian model for the modeling of DRX and PDRX 4

the TRM model implements a particular remeshing procedure strongly influenced by the works in [28, 29], that improves the mesh quality and allows topological events such as grain disappearance or the decomposition of unstable multiple junctions. Of course, remeshing is a very costly procedure in a numerical environment, however, in our context, given the lower mesh density needed to define the interfaces in a proper way comparatively to some front-capturing methods such as the LS-FE model, one should expect a considerably improvement in the computational performance regarding the remeshing procedure, and in general a considerable reduction of the CPU-time needed by the numerical model when compared to the LS-FE approach, see [22] for more information regarding the remeshing procedure of the TRM model.

The TRM model can be extended to model GBM when Stored Energy (SE) and capillarity act simultaneously as driving pressures, for which the velocity \vec{v} describing these mechanisms has to be derived. Similarly, ReX can be simulated through the appearance of new grain boundaries (those delimiting new grains during nucleation), for which a remeshing strategy can be established. The following sections are devoted to the implementation of i. a new velocity term \vec{v} taking into account SE into the dynamics of grain boundaries, along with some necessary changes concerning topological operations that may occur during the modeling of this mechanism (section 3) and ii. a remeshing procedure to include new domains (grains) in the microstructure and the laws governing their apparition as a function of the TMT followed by the material (section 4), where the methodologies proposed in [36] regarding this aspect were used.

3. Grain boundary migration under capillarity and SE driving pressures

The simulation of microstructural evolutions are given by the addition of complex and different phenomena as GG [17, 18, 32, 19, 33], ReX [17, 34, 35, 26, 27, 36, 37] or Zener Pinning (ZP) [38, 39, 40, 41, 42]. In [22], GBM with no influence of SE was used to compare the TRM model to other approaches (LS-FE [35, 18, 19]), the base model used to represent this phenomenon is commonly known as migration by curvature flow. The velocity \vec{v} at every point on the interfaces can be approximated by the following equation:

$$\vec{v}_c = -M\gamma\kappa\vec{n}, \quad (2)$$

where M is the mobility of the interface, γ the grain boundary energy, κ the local magnitude of the curvature in 2D and \vec{n} the unit normal to the grain interface pointing to its convex direction. In an isotropic context as considered here, the terms M and γ are supposed as invariant in space.

Of course when post-dynamic phenomena such as Static ReX (SRX) or Meta-Dynamic ReX (MDRX) are considered, the SE will act as another driving pressure of the GBM. Note that the SE within a grain can be variant, as there could be regions

1
2
3 *A new front-tracking Lagrangian model for the modeling of DRX and PDRX* 5

4 on the grain that have accumulated more or fewer dislocations during the considered
5 thermomechanical treatment (TMT).
6
7

8 At the mesoscopic scale, the SE can be discussed following different hypotheses.
9 Crystal plasticity calculations and EBSD experimental data can bring dislocation den-
10 sity field and so SE field with fine precision until intragranular heterogeneities. While
11 this information is directly usable in pixel/voxel based stochastic approaches such as
12 MC or CA methodologies, generally it is homogenized by considering constant value per
13 grain in deterministic front-capturing (MPF, LS) and front-tracking approaches. If this
14 choice seems quite natural for phenomena where SE gradients and nucleation of new
15 grains are mainly focused on GB like for discontinuous DRX (DDRX), it could be a
16 strong assumption for phenomena where the substructure evolution is important. This
17 aspect was for example studied in [43] in the context of SRX with a FE-LS numerical
18 framework. It was concluded that intragranular gradients on the SE could indeed have
19 a big impact on the grain morphology and that simulations taking into account such
20 variations were more in accordance with experimental observations than simulations
21 using a constant value of SE, but with an important numerical cost as the FE mesh
22 must be then adapted at the intragranular heterogeneities scale. In the following, a con-
23 stant homogenized energy per grain is assumed in a DDRX environment. Nonetheless,
24 the approach presented in this article to model GG with a SE field can be used in the
25 context of a heterogeneous intragranular energy field, this aspect will be investigated
26 in a forthcoming publication and constitutes one of the main originalities of the TRM
27 model, when compared for instance to front-tracking models (like vertex ones) that can
28 not use heterogeneous intragranular field values.
29
30
31
32
33
34
35
36
37

38 Thus, here SE can act on the displacement of the interface by considering the
39 difference of SE at both sides of the interface. We will adopt a slightly modified
40 methodology to the one presented in [34] to quantify it:
41

$$42 \vec{v}_e = -M\delta_{(\dot{\epsilon})}[E]_{ij}\vec{n}, \quad (3)$$

43 where the term $[E]_{ij}$ defines the difference of SE E between the grains i and j
44 ($E_i - E_j$), the term $\delta_{(\dot{\epsilon})}$ is a mobility coupling factor whose nature is explained in [36]
45 appendix c§ and where the direction of the unit normal \vec{n} sets, for a given node of
46 the interface, the order of the indices as: first the index i and then j . Note that this
47 definition holds even if the direction of \vec{n} is ambiguous (in the case of a flat interface
48 with no convex side) as the direction of the velocity \vec{v}_e will be then pointed, in all cases,
49 from the lower to the higher value of SE no matter what the direction of \vec{n} is. Moreover
50 the value of SE can be computed using the equation:
51
52
53
54
55

$$56 E = \frac{1}{2}\mu b^2 \rho, \quad (4)$$

57 § A mobility coupling factor function of the effective strain rate $\dot{\epsilon}$ with $\delta_{(\dot{\epsilon})} = 1$ when $\dot{\epsilon} = 0$.
58
59
60

1
2
3 *A new front-tracking Lagrangian model for the modeling of DRX and PDRX* 6

4 where b corresponds to the norm of the Burgers vector and μ corresponds to the
5 elastic shear modulus of the material.

6 Finally, the contribution of driving pressures due to SE and capillarity can be
7 accounted by linearly adding the two velocities as in [34, 27]:
8

$$9 \quad \vec{v} = -M(\delta_{(\epsilon)}[E]_{ij}\vec{n} + \gamma\kappa\vec{n}), \quad (5)$$

10 where \vec{v} denotes the final velocity of the interface during GBM when SE effects are
11 included.
12

13 3.1. Velocity at multiple junctions

14 Equation 2 can only be used in a one-boundary problem, as in a more general context,
15 the presence of multiple junctions (the intersection points of more than 3 interfaces)
16 makes it impossible to compute a curvature κ or a normal \vec{n} at these points. As ex-
17 plained in previous works [22, 23], we have used an alternative methodology to compute
18 the velocity due to capillarity at multiple points: Model II of [11], where the product
19 $\kappa\vec{n}$ is directly obtained from an approximation of the free energy equation of the whole
20 system in a vertex context.
21

22 Similarly, Eq. 3 only holds in a one-boundary problem as neither the value of $[E]_{ij}$
23 nor the value of \vec{n} can be obtained at these points. To solve this, a different approach
24 has been developed to compute a “resultant” velocity due to store energy \vec{v}_e at multiple
25 junctions. This approach is illustrated in Fig. 1 where for the sake of clarity, the value
26 of M has been held constant and equal to 1. Fig. 1.a shows a typical configuration
27 where the boundaries of three grains converge to a single point, each grain i has its
28 own SE E_i where $E_1 > E_3 > E_2$. The values of the velocity for each normal boundary
29 have been computed with Eq. 3 and are shown as white arrows for each node in the
30 boundary of Fig. 1.b, here the index on the normal \vec{n}_{ij} term is only representative of
31 their direction and serve to set the indices of each $[E]_{ij}$ terms, these expressions do not
32 follow the Einstein notation summation laws, all summations will be represented by the
33 conventional Σ operator.
34

35 If a portion of differential size dr centered at the multiple point is evaluated (see
36 Fig. 1.c) the boundaries between grains will appear as flat, here the difference on the
37 SE can be seen as a distributed difference of potential $[E]_{ij}$ applied on the length of
38 the grain boundary of size dr (analog to a given pressure acting as a resultant force
39 on a given interface). A normal \vec{n}'_{ij} can be obtained and used to compute a velocity
40 of each boundary (1.d) applied at its center. Note that the direction of \vec{n}'_{ij} can be
41 chosen ambiguously on this linear segment, however, as mentioned before, an eventual
42 ambiguity on the direction of \vec{n} do not represent an ambiguity on the term $-[E]_{ij} \cdot \vec{n}_{ij}$
43 as $[E]_{ij} \cdot \vec{n}_{ij} = [E]_{ji} \cdot \vec{n}_{ji}$ with $[E]_{ji} = -[E]_{ij}$ and $\vec{n}_{ji} = -\vec{n}_{ij}$. These velocities can be
44 divided and applied at the ends of each boundary and finally added at the junction
45
46
47
48
49
50
51
52
53
54
55
56
57
58
59
60

A new front-tracking Lagrangian model for the modeling of DRX and PDRX 7

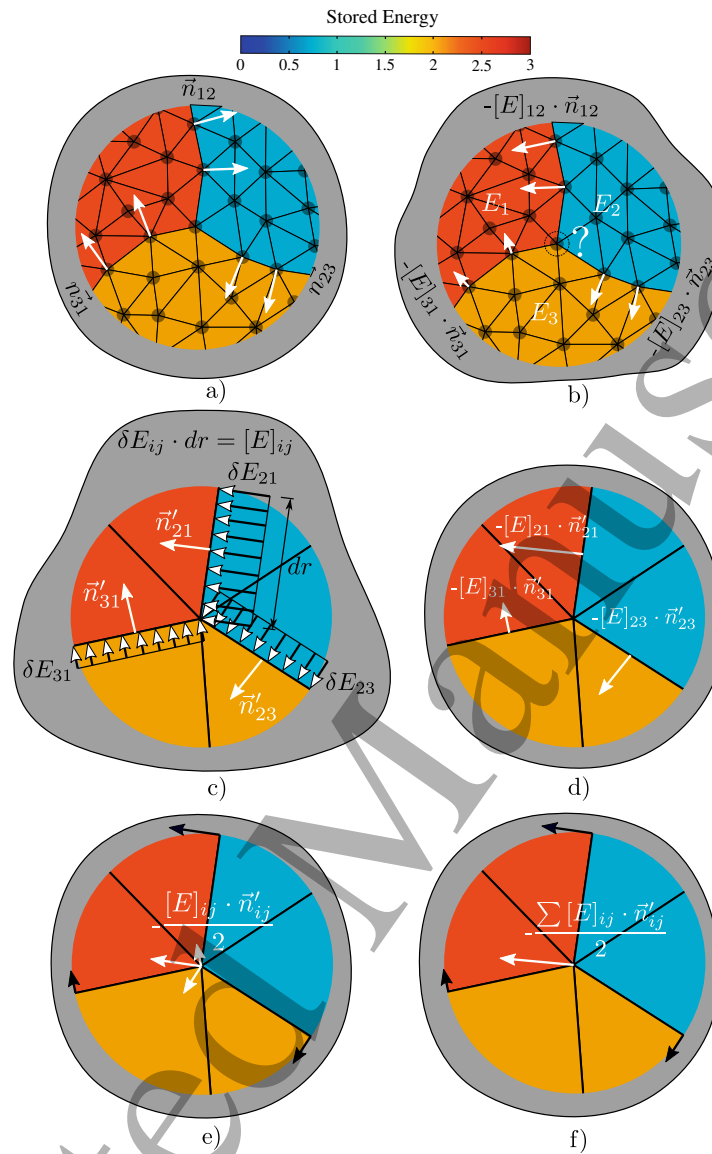


Figure 1: Graphical demonstration of the obtention of Eq. 6, a) typical triple junction configuration with values of SE homogenized on each grain and the normal vectors n computed at the nodes of the interfaces pointing to their convex side, b) computation of the term $-[E]_{ij} \cdot \vec{n}_{ij}$ for each node of the interface except for the node at the triple junction, c) definition of the same configuration as in a) but in a differential portion of radius dr , d) the resultant driving forces are applied at the center of the segments on the differential portion, e) and f) the driving forces are distributed at the ends of each segment and an expression can be formulated at the triple junction for its resultant driving force.

point (Figures 1.e and 1.f respectively) to obtain a valid velocity vector field at multiple junctions. The expression on Fig. 1.f can be extended to the case where the values of

1
2
3 *A new front-tracking Lagrangian model for the modeling of DRX and PDRX* 8

4 M are neither constant nor equal to 1:

$$5 \quad \vec{v}_e = \frac{-\Sigma M \delta_{(\dot{\epsilon})} [E]_{ij} \vec{n}}{2}, \quad (6)$$

6
7
8
9 of course, this expression can be also used in cases of multiple junctions of any
10 order, where more than three interfaces meet. Eq. 6 will be used to compute the value
11 of v_e at multiple junctions as an approximation to the yet unknown behavior of such
12 configurations under the influence of SE in a transient state.

13
14
15 Boundary conditions are also modeled through the use of **Model II**. We do so by
16 changing the status of every L-Node found in the domain boundary to a P-Node. Then,
17 every P-Node of the boundary creates a “virtual” connection (a connection to take into
18 account in **Model II**) to the two adjacent nodes also belonging to the domain boundary.
19 Finally, only the tangent \parallel component of the velocity \vec{v} obtained for these P-Nodes is
20 used in their movement.
21
22
23
24

25 *3.2. Topological changes: capillarity, stored energy*

26
27 Multiple changes in the topology of the microstructure occur during GG and ReX. In
28 general, the topological changes during GG are given by the disappearance of grains:
29 on a shrinking grain, each of their boundaries evolves until they *collapse* to multiple
30 junctions. Eventually, all boundaries collapse to a single multiple junction and the
31 domain occupied by the grain disappears. This behavior was implemented on the
32 original TRM model presented in [22] by means of the application of the *selective node*
33 *collapse* operator, where some restrictions were made regarding the order of collapsing.
34
35

36
37 In [22] we opted to use this methodology to produce coherent topological changes
38 on the microstructure, leading to a series of rules on the *selective node collapse* operator
39 (see section 2.4.1 of [22]). These rules gave to the P-Nodes a higher influence over other
40 kind of nodes and prevented the collapsing of non-consecutive nodes as illustrated in
41 Figures 2 and 3 respectively.
42

43
44 The implementation of such node collapsing strategy allows a high control over the
45 order on which the topological changes occur, unfortunately this kind of reasoning can
46 only be used on isotropic GG and can not be used when SE or spatial heterogeneities
47 of the mobility/interface energy must be taken into account.
48
49

50
51 When considering SE, the kinetics of the GB are not only led by the movement
52 of multiple points; flat surfaces can evolve with a given velocity and it is possible that
53 the velocity of simple boundaries may become much more important than the velocity
54 of multiple junctions. Fig. 4 illustrates this behavior with six grains with a specific
55 SE state. The circular grain in the middle grows due to its low SE compared to the
56 SE of its surrounding grains. The circular grain is indeed surrounded by an initially
57

58 \parallel In this context, the tangent component refers to the tangent of the domain limits and not to the
59 tangent of the GB intersecting the domain boundaries.
60

A new front-tracking Lagrangian model for the modeling of DRX and PDRX 9

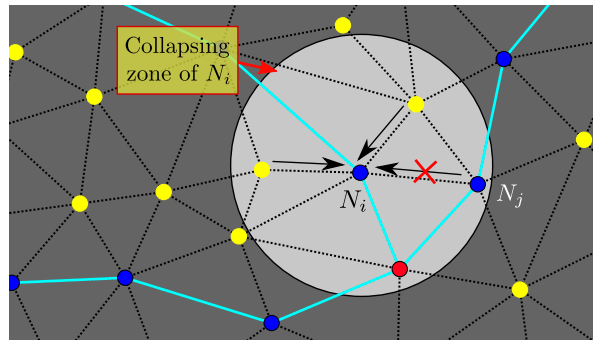


Figure 2: Node Collapsing rule in GG by capillarity. Some nodes are within the collapsing zone of N_i : Two S-Nodes (yellow) will collapse, one L-Node (blue) cannot collapse and one P-Node (red) cannot collapse. N_i cannot collapse P-Nodes (topological degree), N_i can collapse L-Nodes but N_j does not belong to the same line (i.e. they do not belong to the same grain boundary). [22]

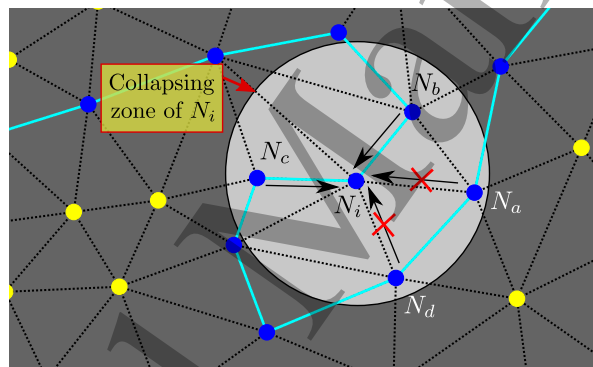


Figure 3: Node Collapsing rule in GG by capillarity. Some nodes are within the collapsing zone of N_i : four L-Nodes (blue) N_a , N_b , N_c and N_d . Only Nodes N_b and N_c can collapse as they are consecutive to N_i within the same line. [22]

squared grain that starts shrinking by the combined effects of capillarity at their external boundaries and the surface taken away by the circular growing grain. Fig. 4.right, shows the moment when the boundary of the circular grain and the external boundaries of the initially square grain collide, unchaining a series of topological changes on the microstructure. These topological changes are illustrated in Fig. 5, where new multiple junctions (Points) appear, grain boundaries (Lines) are split and grains (Surfaces) are divided.

These several changes on the microstructure (contact of different grain boundaries in non-convex grains) can not be accomplished by the TRM model if the rules described above and illustrated by figures 2 and 3 are maintained. This is why these two rules need to be overridden and a new condition implemented: If two non-consecutive nodes (nodes not connected by the microstructural wireframe) collapse, the classification of the remaining node is a P-Node. Additionally, the remaining node is moved to the

A new front-tracking Lagrangian model for the modeling of DRX and PDRX 10

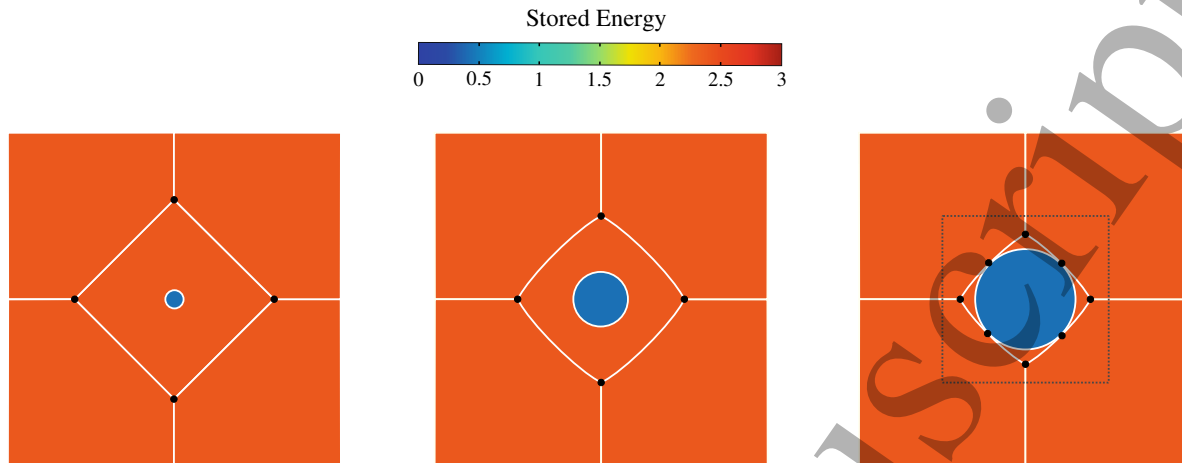


Figure 4: Six grains with a specific SE balance, the circular grain in the middle grows due to its low SE compared to the SE of its surrounding grains. The initially squared grain shrinks by the combined effects of capillarity at their external boundaries and the amount of surface taken away by the circular growing grain. Left: initial state, center: the circular grain grows, right: the boundary of the circular grain and the external boundaries of the initially square grain collide.

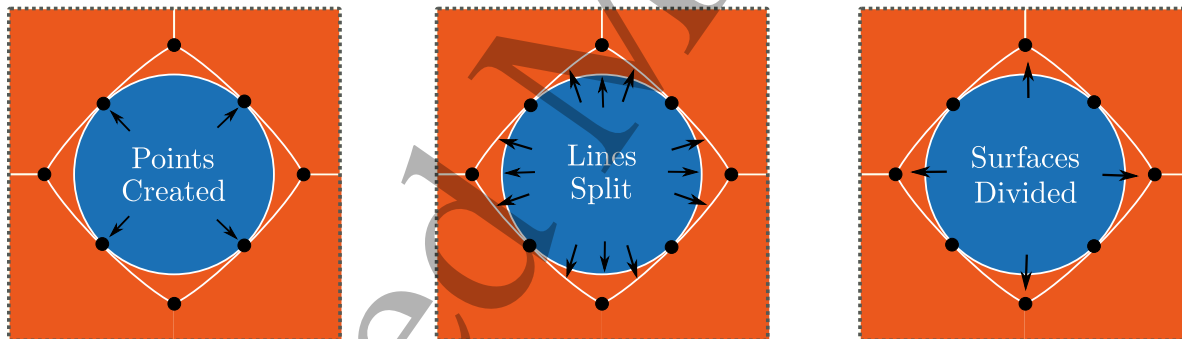


Figure 5: Details of the final event of Fig. 4, highlighting the changes on the microstructure. Here, Points describe multiple junctions, Lines grain boundaries and Surfaces grains.

barycenter of the initial nodes involved in the collapse and the surrounding geometrical entities (points, lines and surfaces) are checked and updated if necessary. Take for example the same configuration shown in Fig. 2 now in Fig. 6: here the collapsing of nodes N_i and N_j is possible, the remaining node N_i is placed in the middle of the edge $\overline{N_i N_j}$ and its classification is changed from L-Node (blue) to P-Node (red). Now their surroundings need to be checked for possible changes on the topology: all three Lines (grain boundaries in cyan) need to erase node N_k as a final/initial point and put in its place P-Node N_i , similarly, one of the lines has to add N_k as a node in their sequence of L-Nodes hence N_k changes also its classification to L-Node.

Similarly, the situation presented in Fig. 3 can be reproduced with the new rules

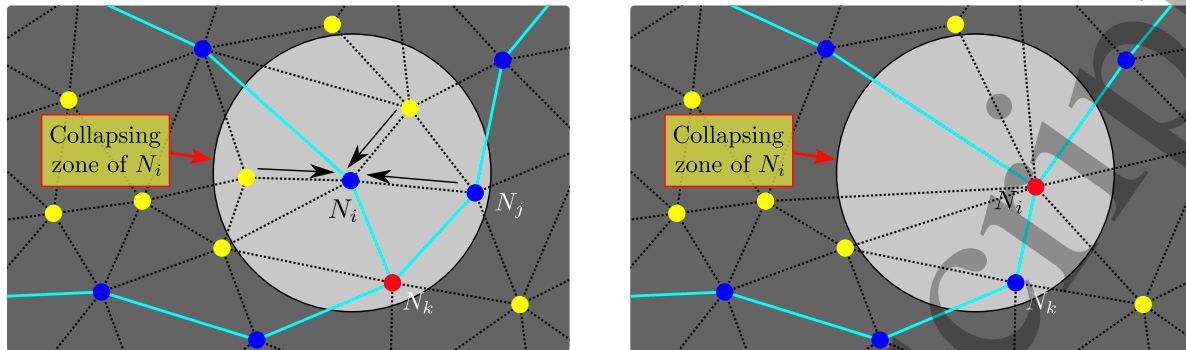


Figure 6: Node Collapsing of Fig. 2 when allowing the collapse between non consecutive nodes, S-Nodes are displayed in yellow, L-Node in blue and P-Nodes in red. The collapsing of nodes N_i and N_j produces a new P-Node (N_i) while the preexistent P-Node N_k needs to be reclassified as a L-Node. Left: initial state, right: state after collapse.

of collapsing: on the initial state (Fig. 7.a), the collapsing zone of N_i puts L-Nodes N_a , N_b , N_c and N_d inside. The first node to be collapsed is L-Node N_a . After this initial collapse (Fig. 7.b) the collapse produces L-Node N_i to be moved to the center of the edge $\overline{N_i N_a}$ and to become a P-Node. Moreover, the collapsing zone of N_i changes its position and leave L-Node N_c out hence it will not be collapsed. Additionally, a new topological change is identified (Fig. 7.c), here the collapse is also responsible for the fact that a Surface is divided in two new surfaces (cyan and orange Surfaces). Finally, the remaining collapses are performed between P-Node N_i and L-Nodes N_b and N_d (Fig. 7.d), these collapses are performed in the conventional way following the rules of collapsing between P-Nodes and L-Nodes presented in [22].

The new node collapsing rules have been implemented in the TRM model and will be used from this point forward in the cases where SE is present. This node collapsing technique will be able to perform the majority of the topological changes in the microstructure. Furthermore, for the purpose of this article, the creation of boundaries by the decomposition of unstable multiple junctions (multiple junctions with more than 3 meeting boundaries) is handled via the decomposition procedure introduced in section 3.2.4 of [22] without any further implementation.

3.3. The TRM algorithm under the influence of capillarity and stored energy

Finally, the algorithm for a time step of the TRM model in the context of isotropic grain growth under the influence of SE and capillarity is presented in Algorithm 1, where the step “Perform Remeshing and Parallel Sequence” corresponds to the parallel implementation of the TRM model presented in [23].

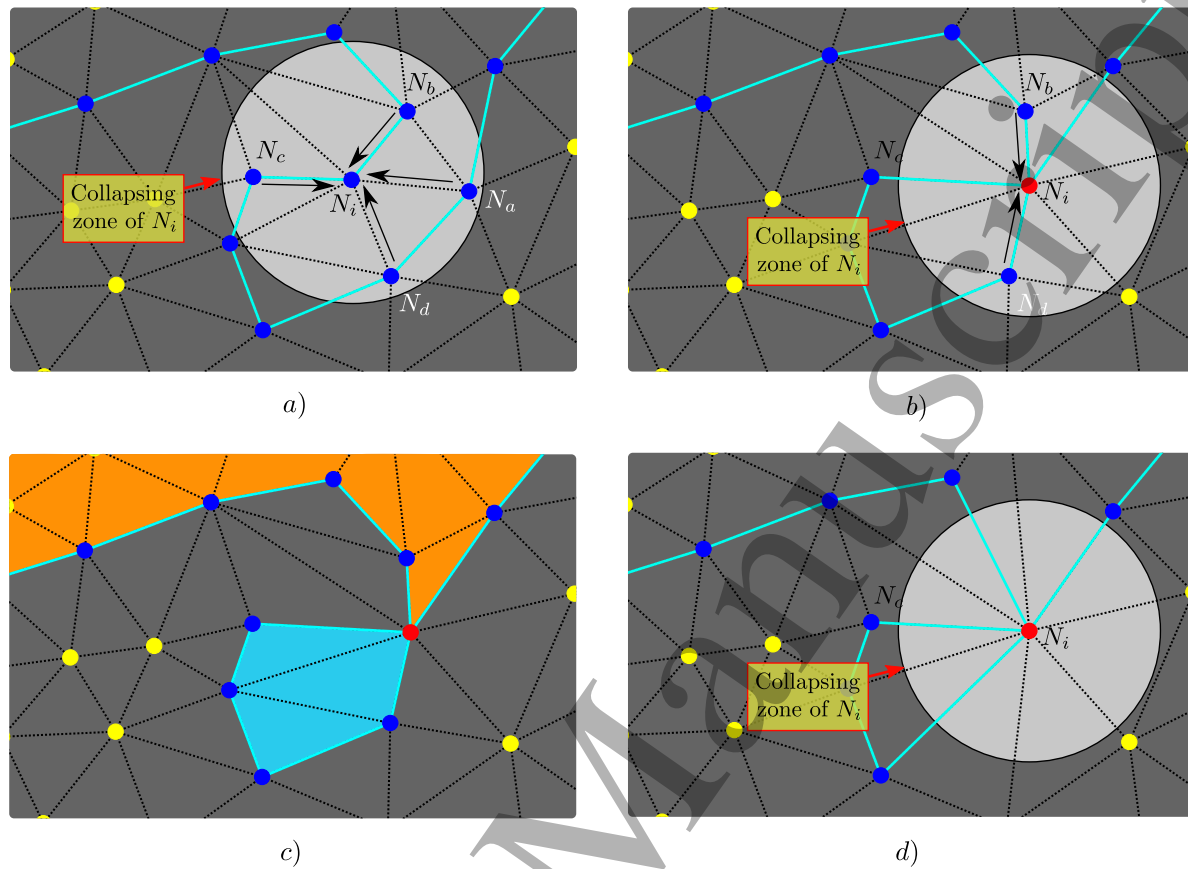


Figure 7: Node Collapsing of Fig. 3 when allowing the collapse between non consecutive nodes, S-Nodes are displayed in yellow, L-Node in blue and P-Nodes in red. a) Initial state; b) L-Node N_i performs the first collapse with N_a . This produces L-Node N_i to be moved to the center of the edge $\overline{N_i N_a}$ and to become a P-Node. Moreover, the collapsing zone of N_i changes its position and leave Node N_c out; c) The collapse also has produced a Surface to be divided in two (cyan and orange Surfaces); d) Additional collapses are performed between P-Node N_i and L-Nodes N_b and N_d , these collapses are performed in the conventional way without moving N_i as it is a P-Node now.

4. Recrystallization

In order to model ReX with the TRM model, two additional components are necessary: the first is a procedure allowing to change the topology of the microstructure and to introduce new grains (i.e. nuclei); the second component is a model for the apparition of nuclei which depends on thermomechanical conditions. Here discontinuous DRX (DDR_X) context is considered. Of course PDRX and subsequent GG phenomena can also be investigated by considering microstructure evolutions when the deformation is completed. The combination of these two mechanisms can describe multiple TMTs that are used today in the material forming industry.

With the purpose of simplicity, in this article we will use the same methodology presented in [36, 44] for the laws governing the introduction of new nuclei during the

Algorithm 1 Isotropic Grain Growth TRM Algorithm for capillarity and SE

```

1: Perform Remeshing and Parallel Sequence
2: for all Points:  $P_i$  do
3:   while Number of Connections  $> 3$  do
4:     split multiple point  $P_i$ .
5:   for all Lines :  $L_i$  do
6:     Compute the natural spline approximation of  $L_i$ .
7:   for all L-Nodes :  $LN_i$  do
8:     Compute curvature and normal ( $\kappa\vec{n}$ ) over  $LN_i$  then compute  $\vec{v}_c$  for  $LN_i$  (Eq 2).
9:     Compute the  $\vec{v}_e$  for  $LN_i$  (Eq 3)
10:  for all P-Nodes :  $PN_i$  do
11:    Compute the product  $\kappa\vec{n}$  over  $PN_i$  using model II of [11] then compute  $\vec{v}_c$  for
12:     $PN_i$  (Eq 2).
13:    Compute  $\vec{v}_e$  for  $PN_i$  (Eq. 6)
14:  Delete Temporal Nodes
15:  for all L-Nodes and P-Nodes :  $LPN_i$  do
16:    Compute final velocity  $\vec{v}$  of Node  $LPN_i$  (Eq. 5)
17:  Iterative movement with flipping check in parallel

```

modeling of hot deformation:

In [36] the evolution of the dislocation density is accounted by a Yoshie-Laasraoui-Jonas Law [45] as follows:

$$\frac{\partial \rho}{\partial \epsilon_{eff}^p} = K_1 - K_2 \rho, \quad (7)$$

which can be evaluated in a discretized time space with an Euler explicit formulation for the next increment step as :

$$\rho^{(t+\Delta t)} = K_1 \Delta \epsilon + (1 - K_2 \Delta \epsilon) \rho^{(t)}, \quad (8)$$

where $\rho^{(t)}$ is the value of the dislocation density at time t and where the value of $\Delta \epsilon$ can be computed as $\epsilon_{eff}^p \cdot \Delta t$ with Δt the time step.

As explained in [36], when a grain boundary migrates, the swept area is assumed almost free of dislocations. This aspect is modeled by attributing to these areas a value of dislocation density equal to ρ_0 , then, for the grains with part of their domain presenting ρ_0 , their dislocation density is homogenized within the grain (as intragranular gradients on the SE are not taken into account either in [36] nor in the present work), the final value of ρ for the growing grains is computed as:

$$\rho^{(t+\Delta t)} = \frac{\rho^t S^{(t)} + \Delta S \rho_0}{S^{(t+\Delta t)}}, \quad (9)$$

1
2
3 *A new front-tracking Lagrangian model for the modeling of DRX and PDRX* 14

4 where S^t and ΔS denote the surface at time t and the change of surface of a given
5 grain.
6

7
8 Additionally to Eq. 9, in PDRX the annihilation of dislocations by recovery must
9 be taken into account. This is done thanks to the following evolution law:

$$11 \quad \frac{d\rho}{dt} = -K_s\rho, \quad (10)$$

12
13 where K_s is a temperature-dependent parameter representing the static recovery
14 term. This recovery law is only taken into account in PDRX as in DRX, Eq. 9 already
15 takes into account the annihilation phenomenon.
16
17

18 19 4.1. Nucleation laws

20
21 The procedure consists in introducing volume (surface in 2D) of nuclei at a rate of \dot{S} ,
22 once the local value of dislocation density has reached a critical value: ρ_c . In [27, 36, 46]
23 this value was obtained by iterating until convergence the following equation:
24

$$25 \quad \rho_c^{(i+1)*} = \left[\frac{-b\gamma\dot{\epsilon} \frac{K_2}{M\delta(\dot{\epsilon})\tau^2}}{\ln(1 - \frac{K_2}{K_1}\rho_c^i)} \right]^{\frac{1}{2}} \quad \text{with } \rho_c^i = \rho_c^{i-1} + c \cdot (\rho_c^{(i)*} - \rho_c^{i-1}), \quad (11)$$

26
27 where i represents the iteration number, c is a convergence factor ($c < 1$ chosen
28 in this article as $c = 0.1$), K_1 and K_2 represents the strain hardening and the material
29 recovery terms in the Yoshie–Laasraoui–Jonas equation discussed in [45], the term $b = 1$
30 in 2D and $b = 2$ in 3D, τ is the dislocation line energy and $\dot{\epsilon}$ is the effective deformation
31 rate used during the deformation of the material.
32
33

34
35 When solving this equation, two special cases may produce an erroneous
36 computation: the first is given when $K_1/K_2*\rho_c > 1$ for which the logarithm is undefined,
37 the solution to this is to limit the value of $\rho_c < K_2/K_1$ whenever this situation occurs.
38 The second is when $\dot{\epsilon} = 0$ which corresponds to the intervals where PDRX is considered.
39 Two solutions may be considered for this situation: the first is to block the nucleation
40 when it is not necessary (metadynamic evolution for example), and the second to supply
41 a value of $\dot{\epsilon} > 0$ to Eq. 11. Here, we have chosen the latter, for which an apparent
42 effective strain rate $\dot{\epsilon}_s$ is used instead $\dot{\epsilon}$ in PDRX:
43
44

$$45 \quad \dot{\epsilon}_s = \frac{\int_0^t \dot{\epsilon}^2 dt}{\int_0^t \dot{\epsilon} dt}, \quad (12)$$

46
47 which accounts for the instant mean value of the real effective strain rate and gives
48 the possibility to produce nucleation immediately after the the deformation stages.
49
50

51
52 Once a value of ρ_c is computed, the surface per unit of time \dot{S} of nuclei to be
53 inserted can be computed with the following equation corresponding to a variant of the
54 proportional nucleation model [47]:
55

$$56 \quad \dot{S} = K_g P_c, \quad (13)$$

57
58
59
60

A new front-tracking Lagrangian model for the modeling of DRX and PDRX 15

where the term K_g is a probability constant depending on the processing conditions and P_c is the total perimeter of the grains whose dislocation density is greater than ρ_c .

Another constraint is given by the minimal radius r^* of nucleation (the radius at which the nuclei should be inserted in the domain so the capillarity forces would not make it disappear) which can be computed thanks to the following equation [48]:

$$r^* = \omega \frac{\gamma}{(\rho_c - \rho_0)\tau}, \quad (14)$$

where $\omega > 1$ is a safety factor ensuring the growth of the nucleus at the moment of its apparition. The term ω accounts for the non-spherical shape of a grain inserted in a discretized domain such as in the TRM model. In section 5.1 a value for this factor will be obtained based on numerical tests.

4.2. Nucleation approach for the TRM model

Having defined the tools needed to obtain the kinetics of the grain boundaries, where the pressure behind such kinetics can be of different nature: capillarity, SE or both. However, in order to model ReX it is necessary to have a way to introduce new grains into the domain of the TRM model. Nucleation, similarly to boundary migration, is one of the ways of the microstructure to relax the high gradients of the SE appearing during or after a TMT. Nucleation has been addressed by several approaches for each methodology able to simulate such behavior: LS-FE methods, rely on the definition of circular LS fields (different from the already defined LS fields occupying the same spatial domain) to form nuclei [49, 36], CA and MC methods change the crystallographic orientation and SE value of some cells [50, 51, 52, 53] in order to nucleate while vertex models form new grains by redefining new vertex and interfaces in the shape of triangles around the preexistent vertex points [15].

In the present work, a remeshing-reidentification procedure will be performed around a central node N_i in order to introduce nuclei. A circular region with center N_i will be drawn and all edges crossed by this circle will be similarly split at the intersection as in [24, 25] by successively applying an edge splitting operation, regardless of the classification of the nodes defining the edge (P-Node/L-Node/S-Node) (see Fig. 8). The classification of the new nodes being placed by the splitting algorithm is as L-Nodes unless the split edge represents a grain boundary, in which case the inserted node will be classified as a P-Node (see Figures 9.b.middle and 9.c.middle). Once all edges are split, a Surface Identification algorithm will be performed over node N_i (see section 2.2.5 of [22]), all identified elements and nodes will be inserted into a new empty Surface defining the nucleus, and extracted from their previous Surfaces (grains), new Lines (grain boundaries) will be built with their respective Points (multiple junctions) if any were formed by the nucleation process and all remaining lines and points inside the new surface will be destroyed (remaining lines and points can appear

1
2
3 *A new front-tracking Lagrangian model for the modeling of DRX and PDRX* 16

4 if the nucleation took place near a grain boundary) see Figures. 9.a, 9.b and 9.c left.
5 However, in a parallel context an additional constraint was added: shared nodes can
6 not be involved in the nucleation process, neither as a central node nor one of the
7 nodes of a split edge. This constraint has been added because of the lack of information
8 (position of the edges to cut) around shared nodes and the performance of the nucleation
9 process (as a great amount of information would be necessary to be transferred to other
10 processors). This constraint should not have a great impact on the general behavior
11 of the model as the domain of each processor (and their shared nodes) is changed by
12 the *Unidirectional Element Sending* algorithm presented in [23] every time step, hence
13 constantly unblocking the restriction to nucleate over the same region.
14
15
16
17
18
19
20
21
22
23
24
25
26
27
28
29
30
31
32
33
34
35
36
37
38
39
40
41
42
43
44
45
46
47
48
49
50
51
52
53
54
55
56
57
58
59
60

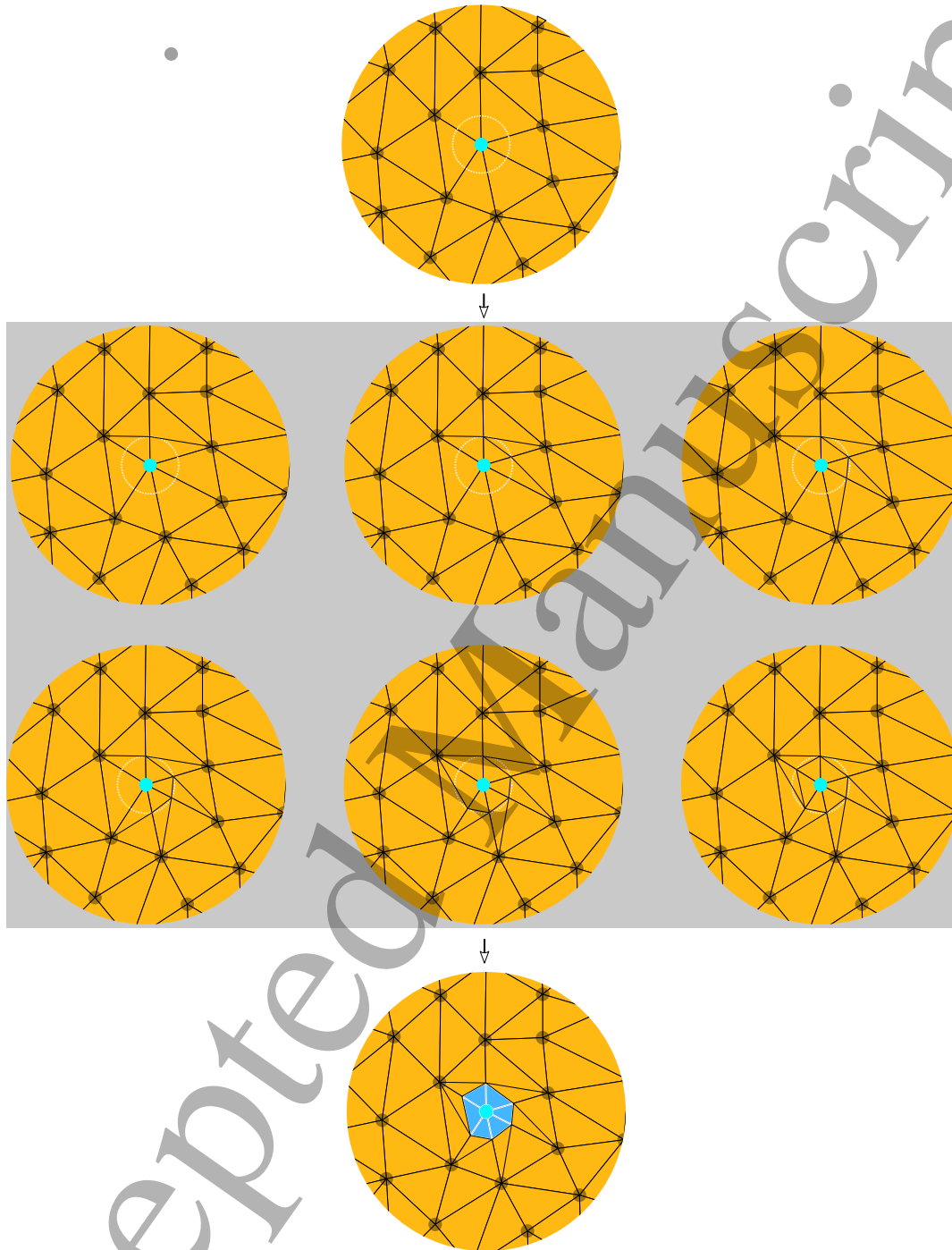


Figure 8: Remeshing steps for the nucleation process of the TRM model. Top: initial state with a selected node (cyan) and a circle drawn over the mesh, middle: successive edge splitting steps to form the interfaces of the nucleus, bottom: the elements inside the nucleus are identified and extracted from its previous Surface container.

1
2
3 *A new front-tracking Lagrangian model for the modeling of DRX and PDRX* 18

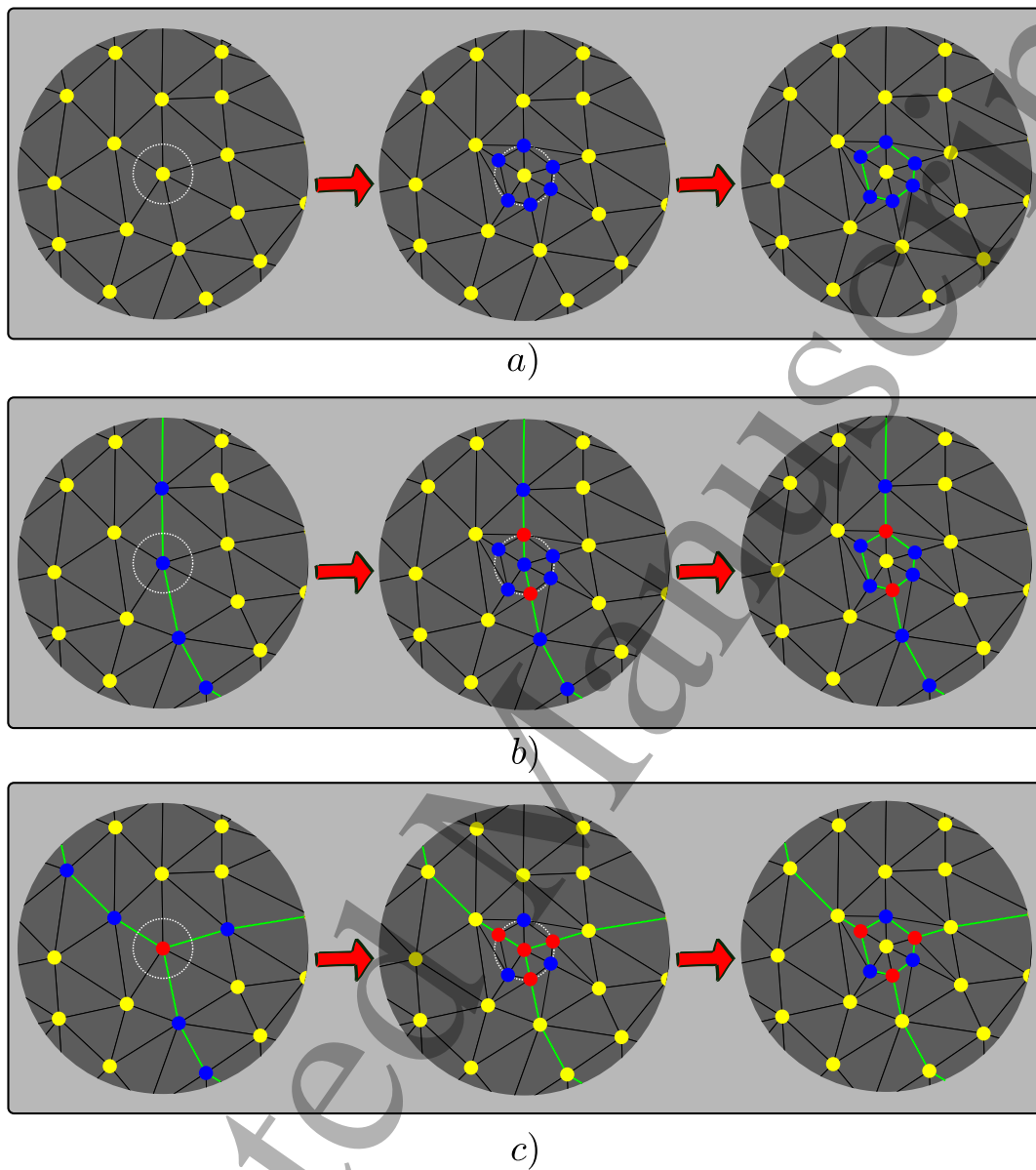


Figure 9: Examples of the formation of nucleus over different types of nodes, a) S-Node at the center and no crossed lines, b) L-Node at the center and one crossed line, two P-Nodes are created, the initial line is divided and two new lines are created, c) P-Node at the center, 3 P-Nodes are created, the P-Node at the center is detached from all its lines and converted to S-Node, 3 new lines are created.

5. Numerical tests

In this section different academic tests will be performed to evaluate the performance of the TRM model when simulating GBM under the influence of capillarity and SE. For these academic tests, dimensionless simulations will be considered. Moreover, the results of simulations using the DRX and PDRX frameworks described in section 4 will be given, these simulations will use the nucleation approach presented in section 4.2 specially developed for the TRM model. The different physical parameters will be taken as representative of the 304L stainless steel. Comparisons with LS-FE predictions will be discussed.

5.1. Circular Grain: competition between capillarity and stored energy

In this test case, it will be evaluated the accuracy of the model when the geometric configuration leads to a competition between the driving forces given by the capillarity and the SE. Here we will adopt a value of boundary energy and mobility equal to $\gamma = 1$ and $M = 1$ respectively. A circular domain with a value of SE $E = \alpha$ is immersed in a squared domain with an attributed value of SE $E = \beta$ (see Figure 10.a and 10.b left) where $\beta > \alpha$. The difference on the SE $[E] = \beta - \alpha$ at the boundary will try to make the circle expand at a rate $v_e = M[E] = [E]$ while the capillarity effect will try to make it shrink at a rate $v_c = M\kappa = \kappa$ where κ is the local curvature. The analytical model for this configuration can be put in terms of a non-linear ordinary differential equation in terms of the radius r of the circle as follows:

$$\frac{dr}{dt} = -\frac{1}{r} + [E], \quad (15)$$

or in terms of the surface S of the circle:

$$\frac{dS}{dt} = 2(-\pi + \sqrt{\pi S}[E]), \quad (16)$$

We have used an Euler explicit approach to solve this equation and the results are used to compare the response of the TRM model for different values of $[E]$ for two cases: the first is given for an initial radius of $r_0 = 0.3$ and the second for $r_0 = 0.025$ (see Figure 10.a and 10.b left). The initial mesh for each one of the two cases is given in Figure 10.a and 10.b right respectively. Note how in the first case, the initial circle boundary is discretized by a number of nodes sufficiently capable of capturing precisely the value of its curvature, hence it will serve to evaluate the accuracy on the kinetics of a typically curved boundary, while in the second case, the circle boundary is only defined by a few nodes allowing to evaluate the behavior of a nucleus when it is inserted on the domain.

Results for this first case are given in Fig. 11 along with the solution of Eq. 16 for different values of $[E]$, Fig. 11.left illustrates how the references curves are superposed to the different simulated curves with a very low error (around 2 % max see Fig. 11.right). Furthermore, the analytic metastable case (given for $[E] = 10/3$) shows a very good

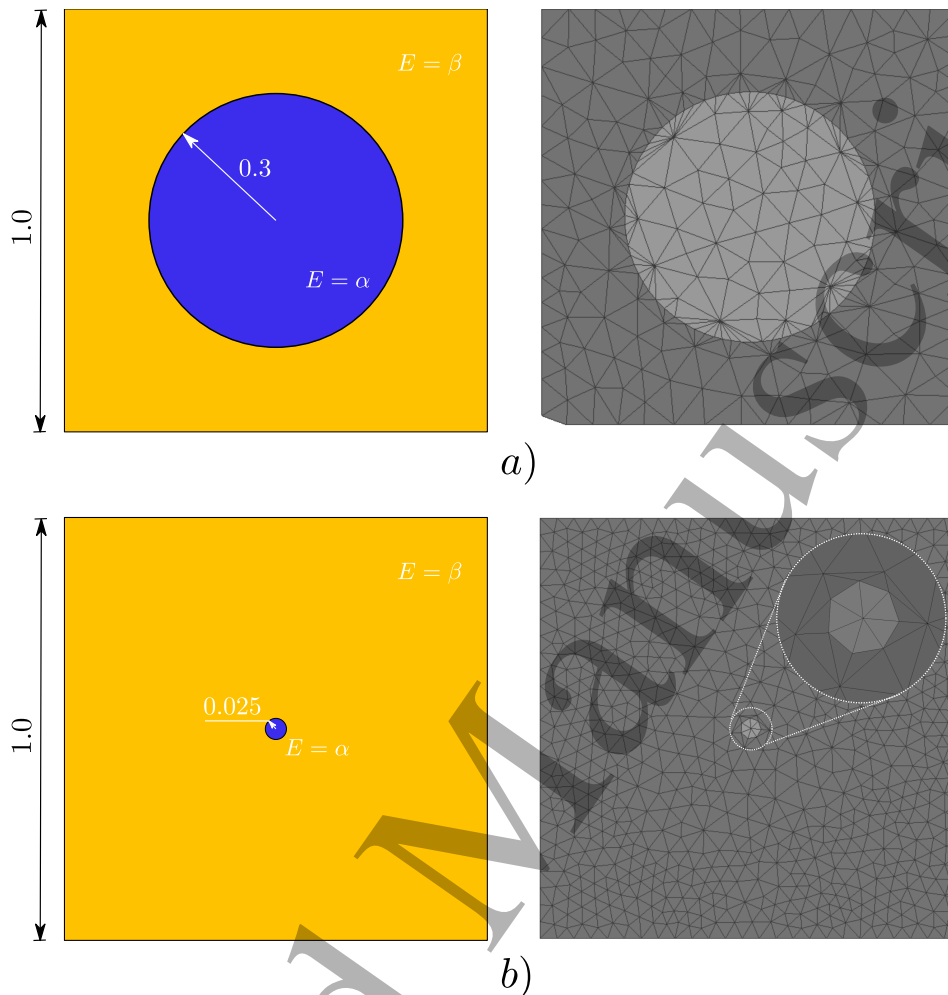


Figure 10: Circle Test, left: initial state and right: initial mesh a) $r = 0.3$ radius (Surface=0.287) b) $r = 0.025$ radius (Surface=0.01963)

behavior losing only 1.2% of its surface at $t = 0.09$.

Similarly, The results for the second circle case are given in Fig. 12. Here it is appreciated how for the cases where the capillarity is the higher driven force ($[E] = 0, 10, 20, 30$), the circle disappears at the good rate. An interesting discussion concerns the case with $[E] = 40$ which corresponds analytically to the metastable configuration. In TRM simulation, the grain disappears. This behavior is due to the low number of nodes at the interface, producing an overestimation on the computed value of its curvature, making it shrink from the very first increment. A value of $[E] \approx 48, 5$ was necessary on the simulated side to maintain a metastable position (an increase of 21.2% accordingly to its analytical value). Moreover, for this value, the error on the prediction of the evolution of the surface was also the highest, going up to 92% after $t = 0.003$. Of course, this error is given as the simulated circle maintains its surface, while the analytical solution shows a continuous increase. The curves corresponding to

A new front-tracking Lagrangian model for the modeling of DRX and PDRX 21

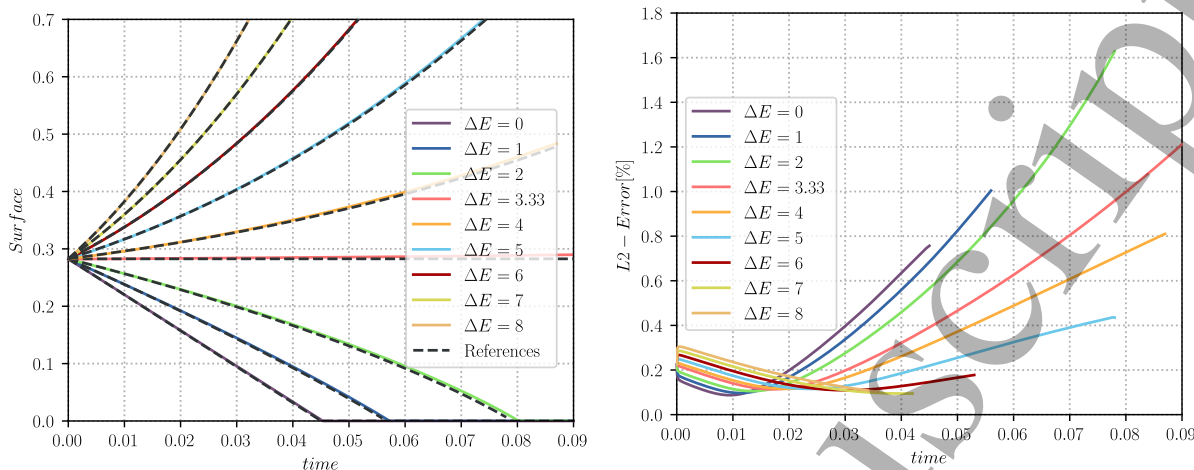


Figure 11: Evolution of the surface (left) and L2 error (right) for the circle test case for an initial circle radius $r = 0.3$ (Surface=0.287) a mesh size $h = 0.006$ and a delta time $dt = 3 \times 10^{-5}$, the analytical results (References) are shown superposed to the simulated curves in black dashed lines. The expected metastable curve is given for a $[E] = 10/3$ (Red curve).

$[E] = 50, 60, 70, 80$ (for which the higher driving force is the SE) show a decreasing error when the value of $[E]$ increases. This result can be used on the determination of factor ω used in Equation 14 where the authors have estimated that a value of $\omega = 1.5$ (which counteracts for an increase of 50% over the analytical value of $[E]$ for a metastable state, see the curve $[E] = 60$ in Fig. 12.) is sufficient in order to give the inserted nucleus a growing state and prevent its early disappearance.

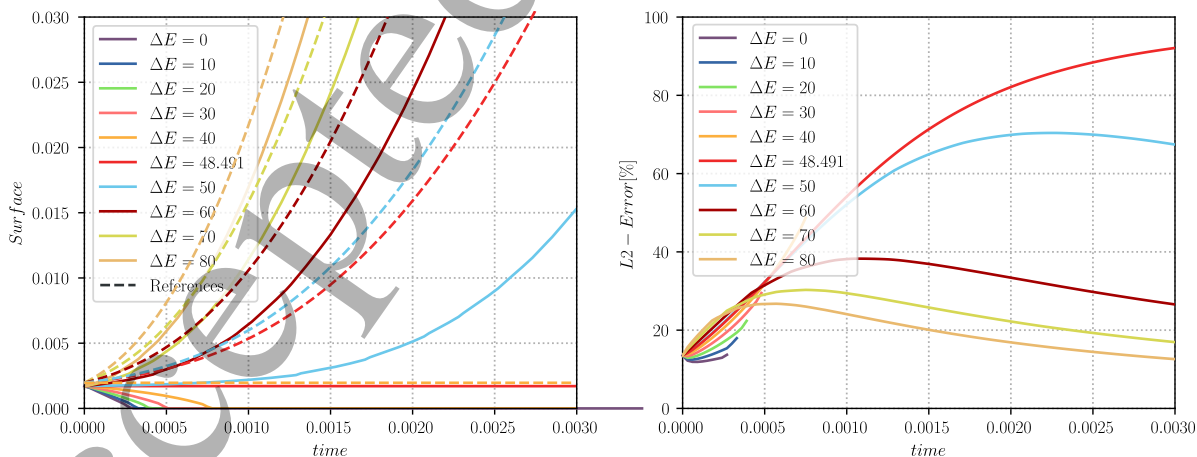


Figure 12: Evolution of the surface (left) and L2 error (right) for the circle test case with an initial circle radius of $r = 0.025$ (Surface=0.01963) a mesh size $h = 0.025$ and a delta time $dt = 1 \times 10^{-5}$, the analytical results (References) are shown as dashed lines of the same color of their corresponding simulated evolution. The expected metastable curve is given for a $[E] = 40$ (orange curve), but metastability was found for $[E] = 48.491$ (Red curve)

5.2. Triple junction : The capillarity effect on the quasi-stable shape of multiple junctions

In [54, 55] analytic solutions for the movement of multiple junctions in a quasi steady-state under the influence of SE were presented. In [54] the so called “Vanishing Surface Tension” (VST) test was introduced to demonstrate the non-uniqueness of the solution presented in [55] hereafter called the “Sharp” solution, this test (the VST test) takes the form of the limit problem given by:

$$\vec{v} \cdot \vec{n} = -M([E]_{ij} + \epsilon\gamma\kappa), \text{ with } \epsilon \rightarrow 0, \quad (17)$$

which has subjected to several 2D test cases and a perturbation analysis to demonstrate that the VST solution corresponds to one of the solutions when $\epsilon = 0$ and to the unique solution otherwise.

These solutions were later studied in [17, 34] using a LS-FE model to obtain the same behavior both in 2D and 3D. Here we have reproduced with the TRM model two tests that show the same behavior as in [54, 17, 34] for the 2D solutions. For all test the “Sharp” solution was obtained when capillarity effects were taken into account (with $\epsilon = 1$) and the VST solution when no capillarity was introduced in the system (hence with a value of $\epsilon = 0$). Furthermore we have developed analytic equations for the evolution of the growing surface in our specific case (see Figure 13), these analytic evolutions are valid up to the point of contact of the multiple junction with the lower edge of the equilateral triangle (the limits of our domain) and allow us to make a more quantitative comparison in terms of error.

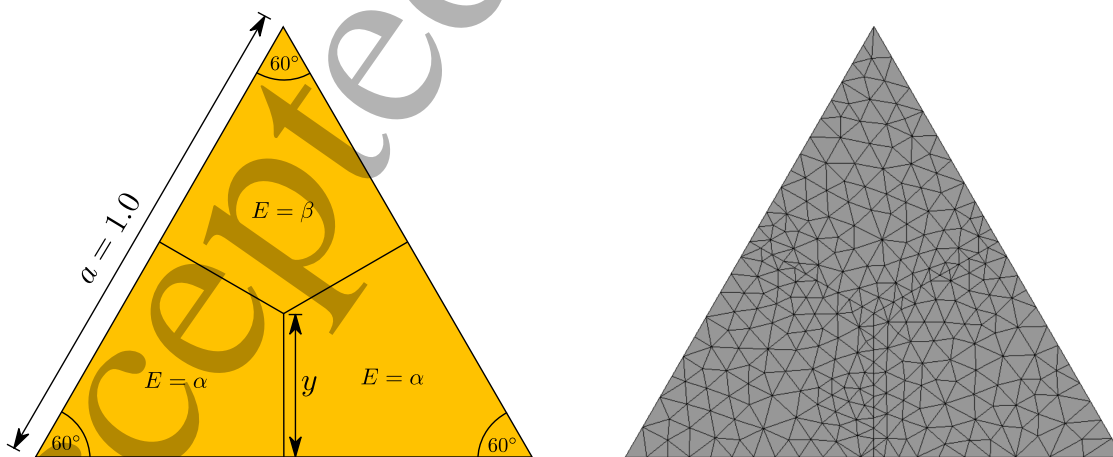


Figure 13: Initial state for the triple junction test, three phases immersed in a domain in the shape of an equilateral triangle, this shape is intended to maintain an orthogonal position of the boundaries with respect of its limits while the configuration evolves. a) Initial configuration and b) initial mesh.

For this test case, the initial conditions are those presented in Fig. 13.left, three

A new front-tracking Lagrangian model for the modeling of DRX and PDRX 23

phases immersed in a domain in the shape of an equilateral triangle, this shape is intended to maintain an orthogonal position of the boundaries with respect of its limits while the configuration evolves. Two of the phases (the two in the lower part of the domain) will have a constant value of SE of α and the third phase a value of $\beta < \alpha$, this configuration will produce a global movement of the triple junction downwards at a constant and normal velocity of the flat interfaces equals to $\alpha - \beta$. Eventually the triple point will reach the bottom part of the domain making it to split and evolve towards a lower energy state; even though this portion of the simulation is showed in some of the results it is not relevant to our study, hence we will give quantitative results up to the point of splitting. The initial mesh for every test performed is shown in Fig. 13.right corresponding to a mesh size parameter of $h_{trm} = 0.006$. Furthermore, values for the boundary energy and mobility have been set to $\gamma = 1$ and $M = 1$ respectively.

The analytic solution for the evolution of the surface of the upper phase (the growing phase) for the Sharp solution is given by:

$$S_{Cap} = \left(\frac{2a}{\sqrt{3}} - y \right)^2 \frac{\sqrt{3}}{4} \quad (18)$$

where a is the length of one of the sides of the equilateral triangle (here $a = 1$) and y is the vertical position of the triple junction measured from the base of the triangle and given by the following expression:

$$y = \frac{a}{2\sqrt{3}} - |\vec{v} \cdot \vec{n}| \frac{2t}{\sqrt{3}} \quad (19)$$

where t is the time and the expression $|\vec{v} \cdot \vec{n}|$ is the instant normal velocity of the flat phase boundaries, i.e. $\alpha - \beta$.

Similarly the analytic response of the VST solution in terms of surface for the growing phase is given by

$$S_{NoCap} = S_{Cap} + \left(\frac{\pi}{6} - \frac{1}{\sqrt{3}} \right) (|\vec{v} \cdot \vec{n}|t)^2. \quad (20)$$

Two test were performed: one with $\beta = 2$ and $\alpha = 4$, i.e. $|\vec{v} \cdot \vec{n}| = [E] = 2$ and one with $\beta = 10$ and $\alpha = 20$, i.e. $|\vec{v} \cdot \vec{n}| = [E] = 10$. The two tests were performed with a time step $\Delta t = 1 \cdot 10^{-5}$. Results for the evolution of the mesh and the surface are given in Fig. 14 for the first and the second cases. It is clear that the accuracy on the scalability of the solution is very good as Figures 14.a, .b and .c are almost equal to the ones of figures 14.e, .f and .g respectively which were obtained for a velocity 5 times higher. Note that the only different frame is given for Figures 14.d.right and 14.h.right as here the capillarity effects over the limits of the domain are not negligible and in Fig. 14.d right the configuration have had 5 times more time to evolve to its given state.

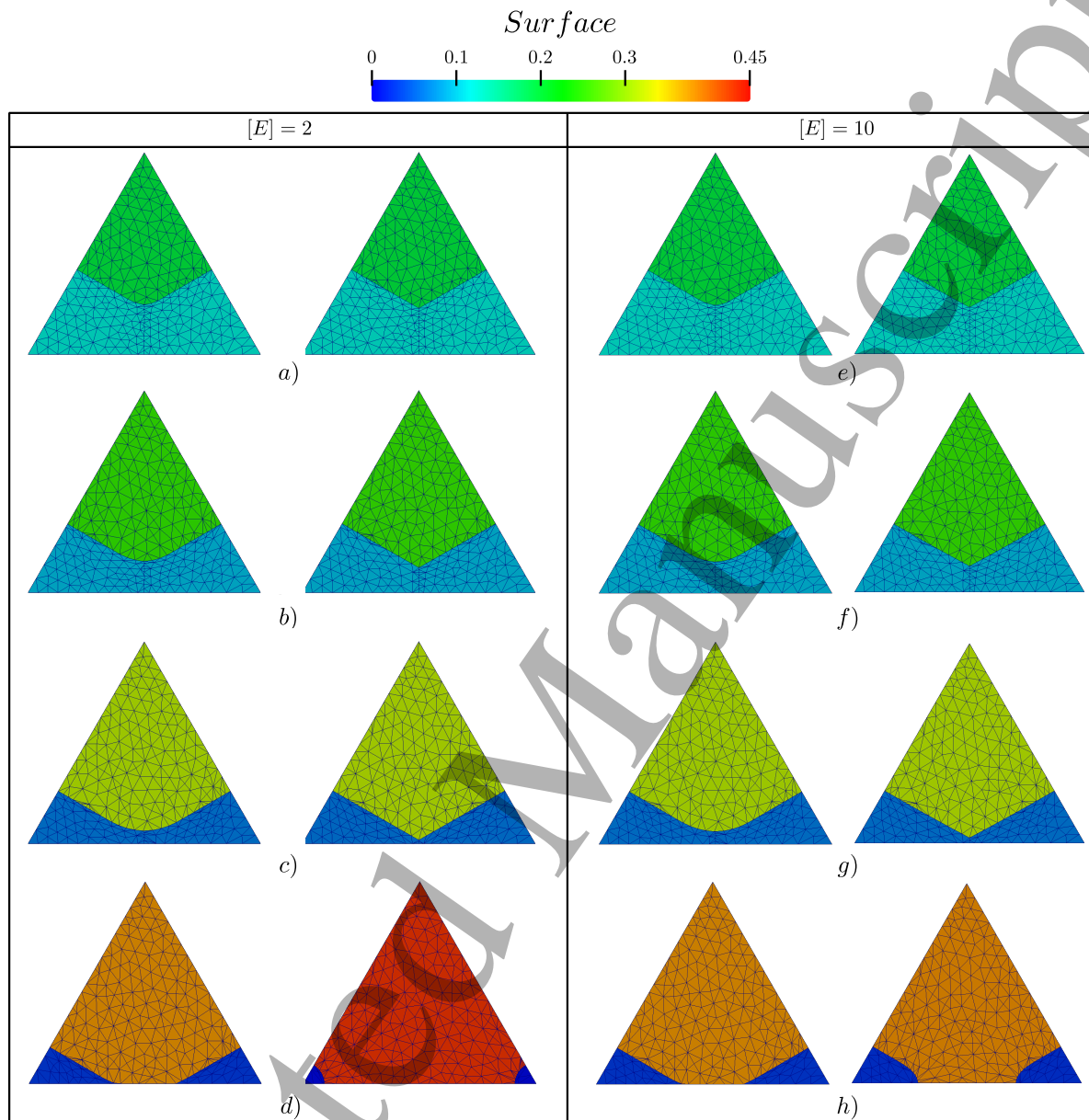


Figure 14: States for the triple junction test case with a value of $[E] = 2$ and $[E] = 10$, for each case, left: with $\epsilon = 0$ and right: with $\epsilon = 1$. for the case with $[E] = 2$ at a) $t = 0.02$ b) $t = 0.04$, c) $t = 0.06$, d) $t = 0.08$. and for the case with $[E] = 10$, e) $t = 0.004$ f) $t = 0.008$, g) $t = 0.012$, h) $t = 0.016$.

The evolution of the surface of the growing phase and its error with respect to equations 18 and 20 is given in Fig. 15, where the L2-Error for both cases was lower than 0.8%.

5.3. DRX/PDRX case

Here a simulation with a few initial grains will be performed using the recrystallization method mentioned in section 4: the initial tessellation will be realized thanks to a

A new front-tracking Lagrangian model for the modeling of DRX and PDRX 25

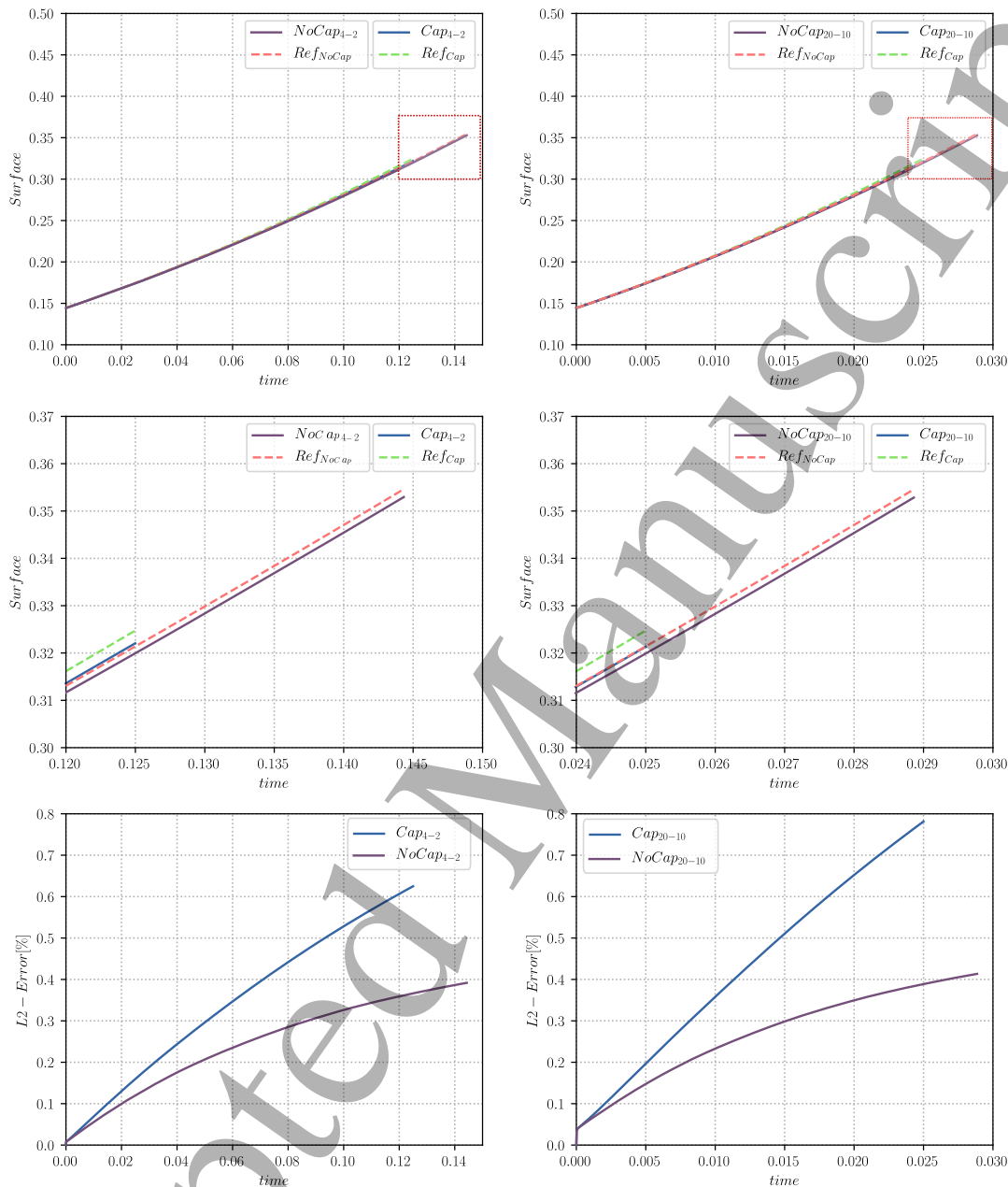


Figure 15: Evolution of the surface of the growing phase of the triple junction test case, from top to bottom: (top) Evolution of the surface, (center) Zoom in the red zone, (bottom) L_2 -error over the evolution of the surface. Left: results for the test with $[E] = 2$ and right: with $[E] = 10$

Laguerre-Voronoi cells generation procedure [56, 57, 58] over a rectangular domain of initial dimensions 0.65×0.328 mm (see Fig. 16) and the values for M , γ , τ and k_s are chosen as representative of a 304L stainless steel at 1100 °C (with $M = M_0 * e^{-Q/RT}$ where M_0 is a constant $M_0 = 1.56 \cdot 10^{11}$ mm⁴/Js, Q is the thermal activation energy $Q = 2.8 \cdot 10^5$ J/mol, R is the ideal gas constant, T is the absolute temperature $T = 1353$ K, $\gamma = 6 \cdot 10^{-7}$ J/mm², $\tau = 1.28331 \cdot 10^{-12}$ J/mm and $k_s = 0.0031$ s⁻¹ [27, 36]). Addi-

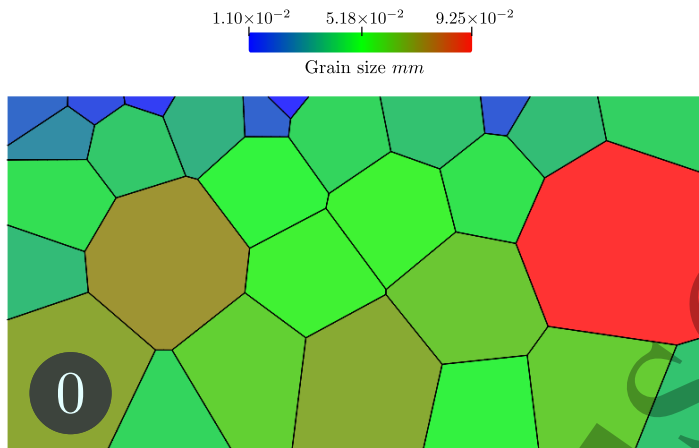


Figure 16: Initial State for the DRX/PDRX test case.

tionally, the parameters K_1 , K_2 , K_g and δ are taken as dependent of the absolute value of the component xx of the strain rate tensor $\dot{\epsilon}$ ($|\dot{\epsilon}_{xx}|$) which is defined as corresponding to a plane deformation case. These parameters will be obtained using a linear interpolation of the values presented in Tab. 1.

Table 1: Parameter data table for the DRX PDRX test case, when in range $|\dot{\epsilon}_{xx}| = [0.01, 0.1] s^{-1}$ the values are interpolated. If $|\dot{\epsilon}_{xx}| > 0.1$ the value for the corresponding parameter will be the same as for $|\dot{\epsilon}_{xx}| = 0.1 s^{-1}$, the same strategy applies when $|\dot{\epsilon}_{xx}| < 0.01$.

$ \dot{\epsilon}_{xx} s^{-1}$	$K_1 mm^{-2}$	K_2	$K_g mm \cdot s^{-1}$	δ
0.01	$1.105 \cdot 10^9$	9	$1.3 \cdot 10^{-4}$	0.937
0.1	$1.55 \cdot 10^9$	6.9	$9 \cdot 10^{-4}$	2.245

Moreover, during PDRX ($|\dot{\epsilon}_{xx}| = 0$), the parameter δ will take the value of 9.18 following the findings in [59]. Also, as explained in section 4.1, during PDRX the parameter ρ_c will be computed using the apparent effective strain rate $\dot{\epsilon}_s$ (see Eq. 12 and Fig. 17.right) instead of the effective strain rate $\dot{\epsilon}$ (equals to 0 in this regime). Finally, outside the range of interpolation, the values are computed as follows: if $|\dot{\epsilon}_{xx}| > 0.1$ the values of all parameters will take the same values as for $|\dot{\epsilon}_{xx}| = 0.1 s^{-1}$, similarly, the same strategy applies when $|\dot{\epsilon}_{xx}| < 0.01$, using the values for $|\dot{\epsilon}_{xx}| = 0.01 s^{-1}$.

Moreover, following the same nucleation approach of [36, 44], here *necklace* nucleation will be used, corresponding to a random distribution of nuclei over the grain boundaries and multiple junctions of grains with a dislocation density higher than the critical value ($\rho > \rho_c$), given by Eq. 11. Note that the rate of surface to introduce by nucleation given by Eq. 13 depends on the perimeter of the grains with $\rho > \rho_c$. Other

types of nucleation could be considered, such as *bulk* nucleation where the nucleus appear at random inside the grains with $\rho > \rho_c$, nonetheless this will not be studied in this article.

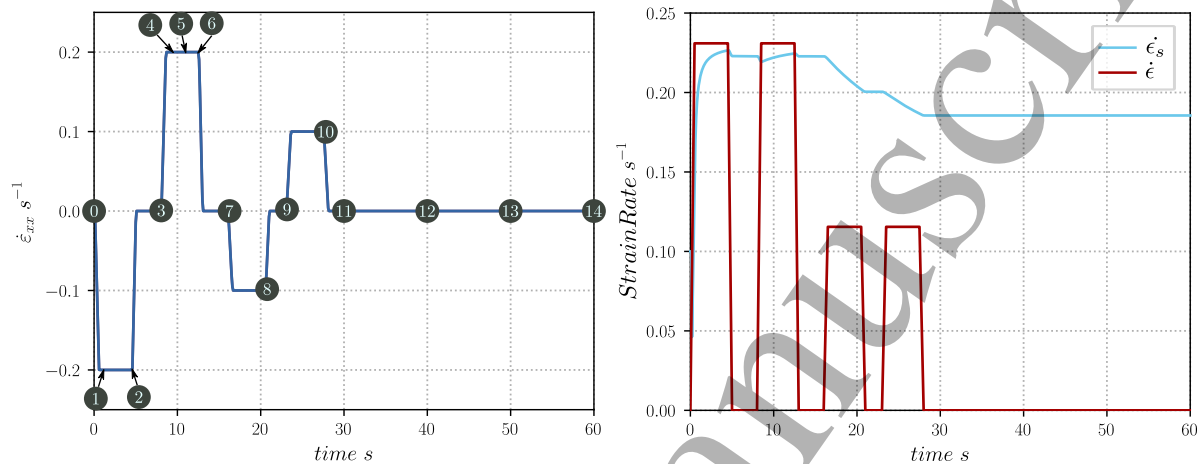


Figure 17: Deformation loading strategy for the DRX and PDRX case: right: the computed values of the effective strain rates $\dot{\epsilon}_s$ and $\dot{\epsilon}$, left: the strain deformation component $\dot{\epsilon}_{xx}$, where multiple markers have been drawn, corresponding to different states during the simulations.

Four cycles of deformation/coarsening will be applied as illustrated in Fig. 17, Fig. 17.right shows the computed values of the effective strain rates $\dot{\epsilon}_s$ and $\dot{\epsilon}$, while Fig. 17.left shows the strain deformation component $\dot{\epsilon}_{xx}$, where multiple markers have been displayed, these markers correspond to different states along with the simulation that will be useful when analyzing the results.

Statistical comparisons of the TRM model and the response obtained by a FE-LS approach presented in [17, 18, 36, 60] will be given. This approach uses a more classic method of mesh adaptation during calculations where the interfaces are captured with an anisotropic non-conform local refined mesh. This methodology will be denoted in the following as the Anisotropic Meshing Adaptation (AMA) model.

A well-known behavior of full-field simulations of microstructural evolutions is that the reduced mobility (γM product) is classically impacted by the choice of the numerical method and is not only a universal physical parameter. This is given by the fact that the motion of multiple junctions depend on a value of velocity that is ill defined at these points. This makes it that different numerical models, use different ways of solving these issues. This, of course, produce a different kinematics during the transient state of multiple junctions, that, even though go in the same direction (for the two approaches used in the manuscript, the TRM and the FE-LS) it produces a higher velocity in the case of the LS-FE approach. In other words, the reduced mobility is a physical param-

1
2
3 *A new front-tracking Lagrangian model for the modeling of DRX and PDRX* 28

4
5 eter that needs to be identified comparatively to experimental data. This identification
6 may lead to different values depending generally of the numerical method used [53]. In
7 [22], the reduced mobility was adjusted in order to minimize the L2-difference between
8 the mean grain size evolution curves considering TRM or AMA numerical strategies.
9 The same methodology was used here in the global thermomechanical paths leading to
10 an increase of 40% in the optimal identified reduced mobility.
11
12

13
14 Here, we have chosen the AMA case as a reference even though there is no way
15 to know which model gives the most accurate response to the given physical problem;
16 this choice on the other hand is given as an example of how the TRM model can indeed
17 obtain similar responses to well-established models in the field of microstructural evo-
18 lutions.
19
20

21
22 Multiple microstructural states have been retrieved from the results given by the
23 TRM model. These states are marked with numbers corresponding to the states of
24 figure 17:
25
26

27 States 1 to 3 are given in figure 18, here state 1 illustrates the apparition of the
28 firsts nuclei in the positions where the dislocation density field reaches its value $\rho \geq \rho_c$.
29 Then state 2 gives the end of the first stage of deformation where more nuclei have
30 appeared, note that the value of the SE in some of the small grains is different from
31 others, these grains have been present longer in the domain and consequently have been
32 subjected to strain hardening, contrary to the nucleus that have appeared later, during
33 or at the end of this deformation stage. Finally state 3 shows the end of the first grain
34 coarsening stage where nuclei have been given time to growth as a product of the high
35 difference in energy with their surroundings.
36
37
38
39

40 States 4 to 6 are presented in Fig. 19. In stage 4 only a small percent of the do-
41 main have a dislocation density of at least ρ_c and nucleation is restricted to these zones,
42 contrary to stage 5, where a bigger part of the domain have reached the value of ρ_c ,
43 consequently new grains appear everywhere. Finally, the end of the second deformation
44 stage is given in state 6 where the first peak of number of grains is reached (4250 grains).
45
46
47

48 States 7 to 10 are given in figure 20, these steps are representative of the ends of the
49 third and fourth deformation/coarsening cycles, where during the deformation the nu-
50 cleation process increases the number of grains while in the grain coarsening stages the
51 high value of the parameter δ (2.245 to 9.18 its dynamic vs its static value) makes the
52 grain number decrease rapidly (see figure 25.a for the evolution of the number of grains).
53
54
55

56 States 11 to 14 are provided in figure 21, these states correspond to a value of time
57 t of 30, 40, 50 and 60 seconds respectively. In this range of time no deformation is
58 considered. Note how the limits of the scale in figure 21 change as a product of the
59
60

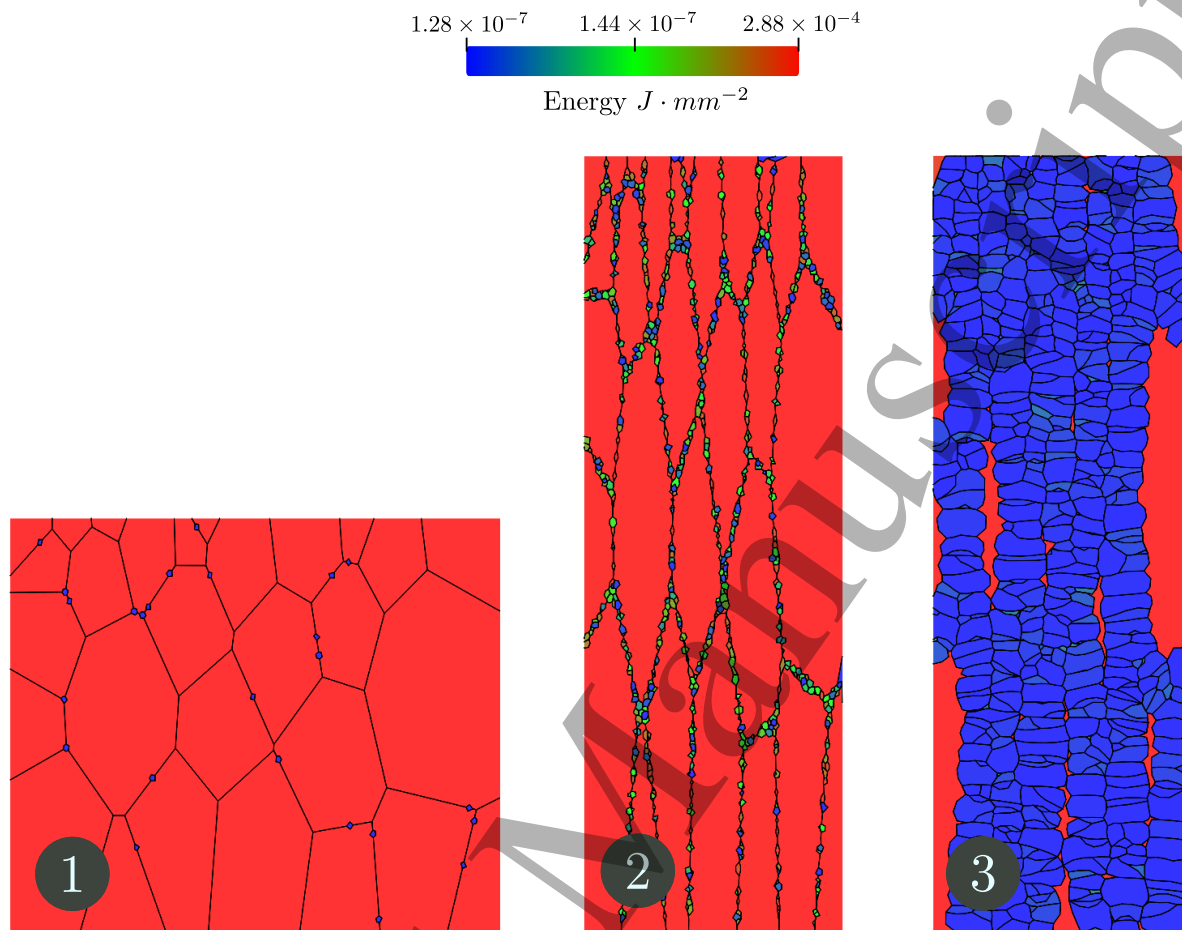


Figure 18: States 1 to 3 (see figure 17) obtained with the TRM model. 1: the first nuclei appear, 2: end of the first stage of deformation, 2: end of the first grain coarsening stage.

disappearance of high energetic grains and to the annihilation of dislocations simulated through equation 10.

Statistical values for the states 4 to 6 and 11 to 14 are given in figures 23 and 24 respectively. The grain size distributions for the TRM model without a mobility increase and with a mobility increase of 40% have been plotted along with the response given by the AMA case. Similarly the evolution of the mean grain size are provided for all simulations in figure 22.left and the L2-difference to the AMA case is given in figure 22.right

Finally, the evolution of some representative values are given in Fig. 25: the evolution of the number of grains, the recrystallized fraction, the mean value of ρ pondered in surface ($\bar{\rho}$) and the total perimeter of the grains whose dislocation density is greater than ρ_c (P_c) are provided.

These results show a good agreement between the general behavior of the TRM

A new front-tracking Lagrangian model for the modeling of DRX and PDRX 30

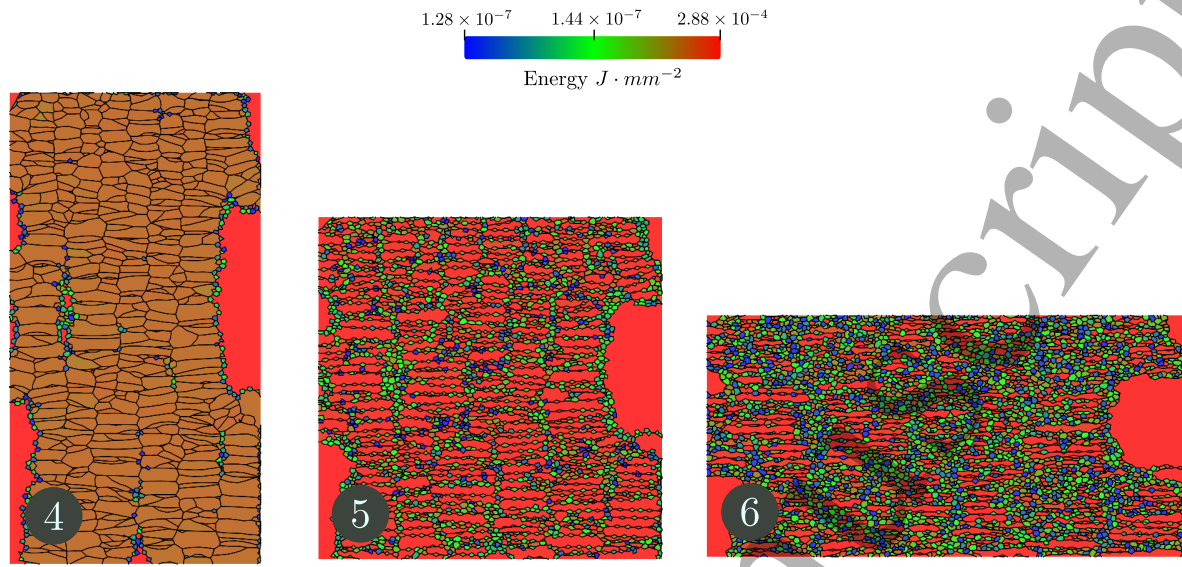


Figure 19: States 4 to 6 (see figure 17) obtained with the TRM model. 4: the nuclei appear on the regions where $\rho > \rho_c$, 5: all the domain is now above the value of ρ_c hence the nucleation occurs everywhere, 6: end of the second stage of deformation, here the maximum number of grains is reached (4250 grains).

model and the behavior of the AMA simulation when an increase of 40% is considered to the reduced mobility $M\gamma$ value (following the findings of [22]). The computational cost for the different iterations of the TRM model is given in Fig. 26, where for the slower simulation the time needed for its completion was of 25 min while the fasted took 20 min, a very small CPU-time compared to the time needed in the AMA case (4 hours and 38 min).

A new front-tracking Lagrangian model for the modeling of DRX and PDRX

31

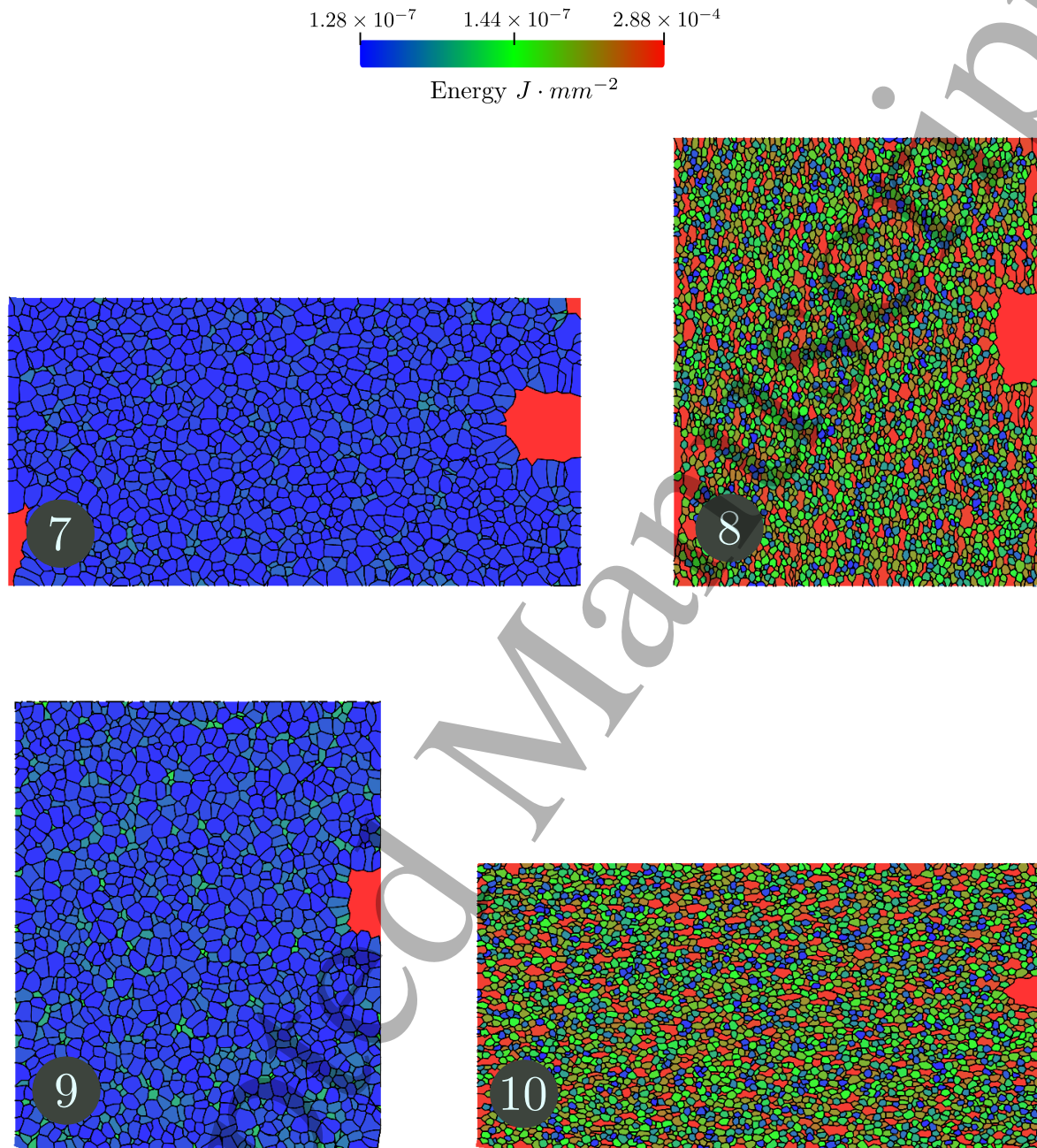


Figure 20: States 7 to 10 (see figure 17) obtained with the TRM model. 7: end of the second grain coarsening stage, the number of grains drops very quickly given by the increase of the value of δ from 2.245 to 9.18 (its dynamic vs its static value) , 8: end of the third deformation stage, 9: end of the third grain coarsening stage, 10: end of the fourth deformation stage.

A new front-tracking Lagrangian model for the modeling of DRX and PDRX 32

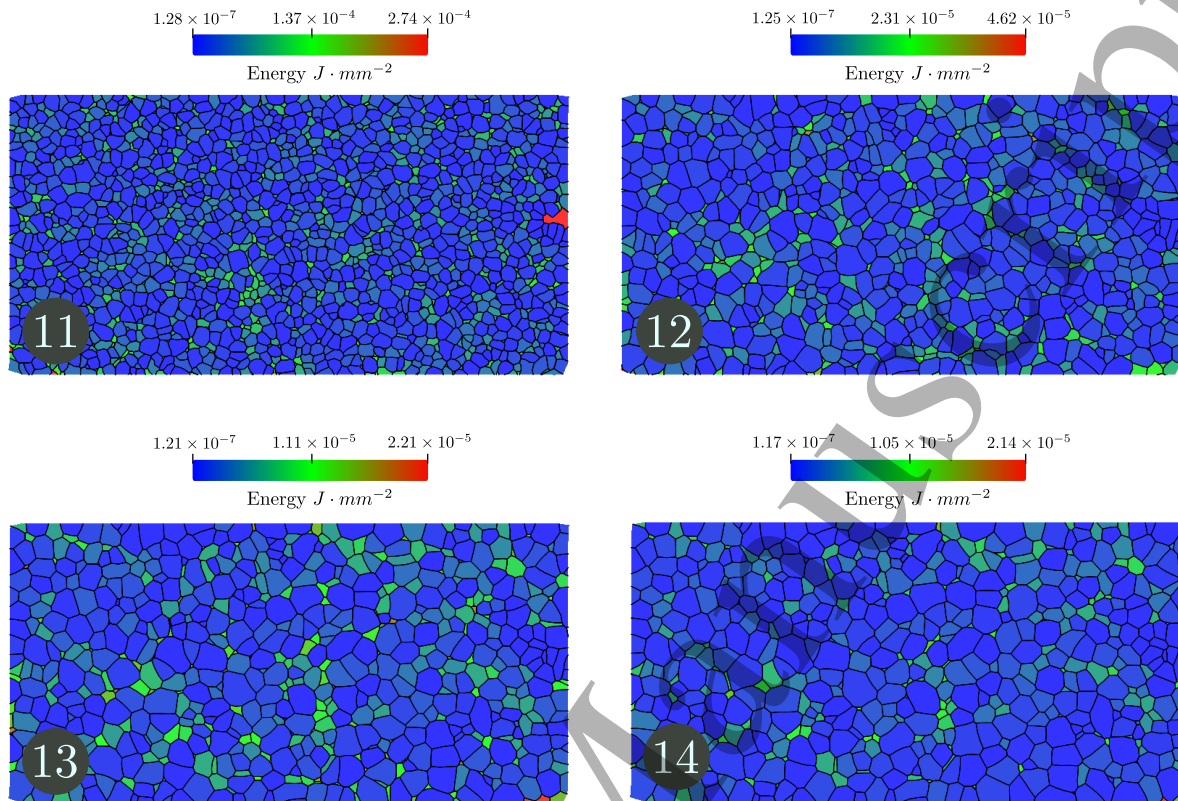


Figure 21: States 11 to 14 (see figure 17) obtained with the TRM model. these state correspond to a value of time t of 30, 40, 50 and 60 seconds respectively.

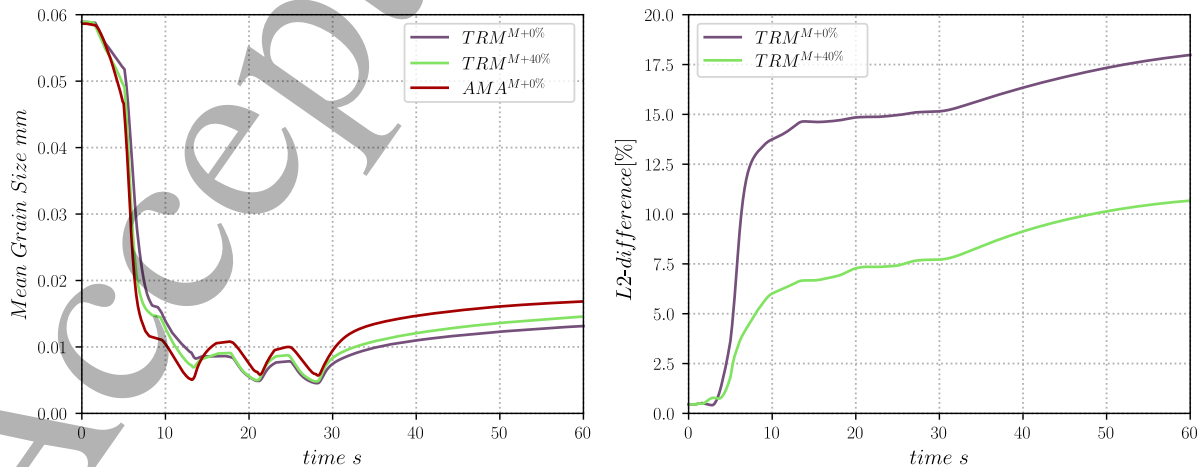


Figure 22: Evolution of the Mean grain size (left) for the TRM model and the L2-difference with the AMA simulation (right).

A new front-tracking Lagrangian model for the modeling of DRX and PDRX

33

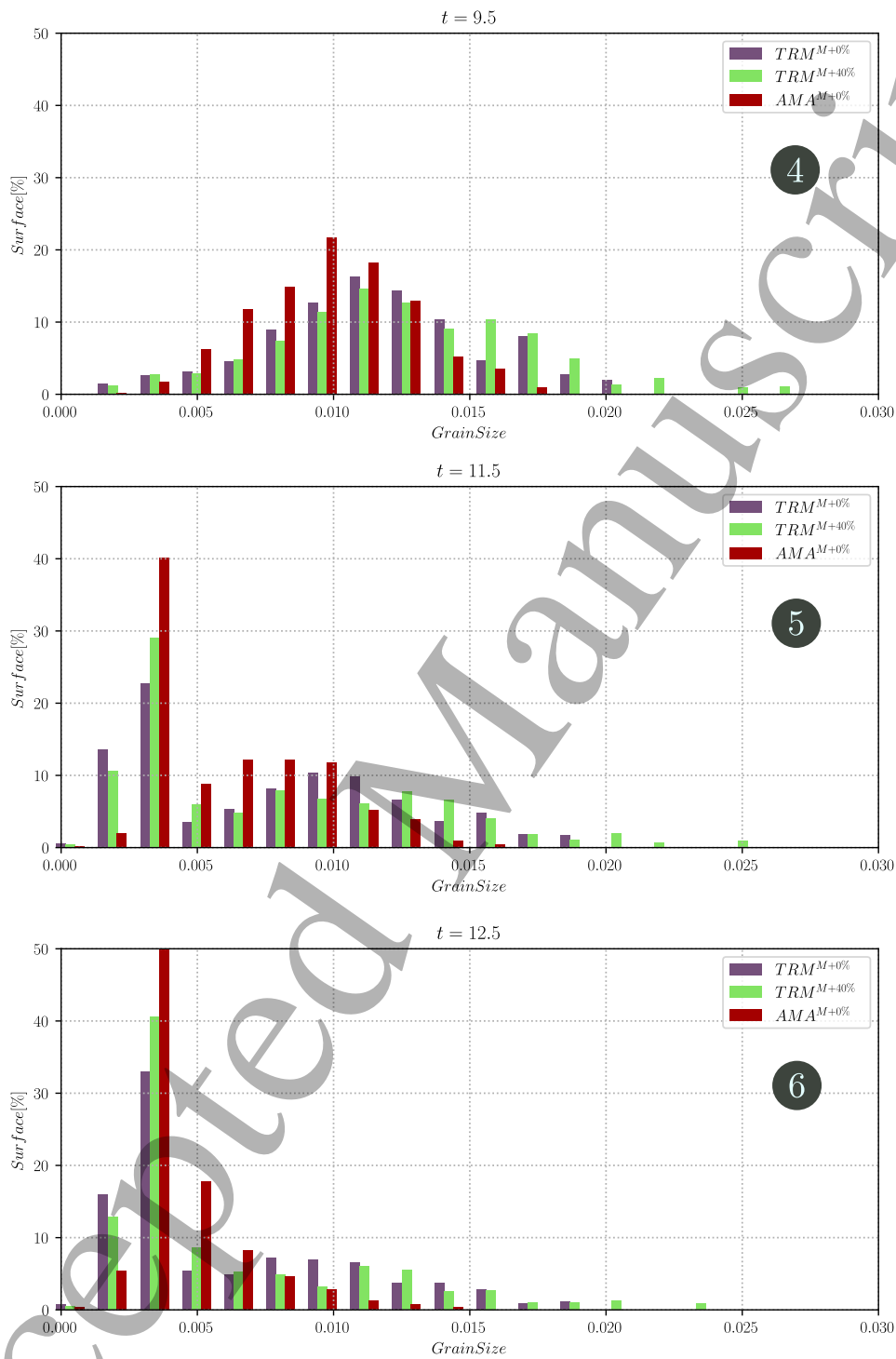


Figure 23: Grain size distributions pondered in surface for the states 4 to 6 (example of a deformation Stage). A peek on the nucleus size can be observed.

A new front-tracking Lagrangian model for the modeling of DRX and PDRX 34

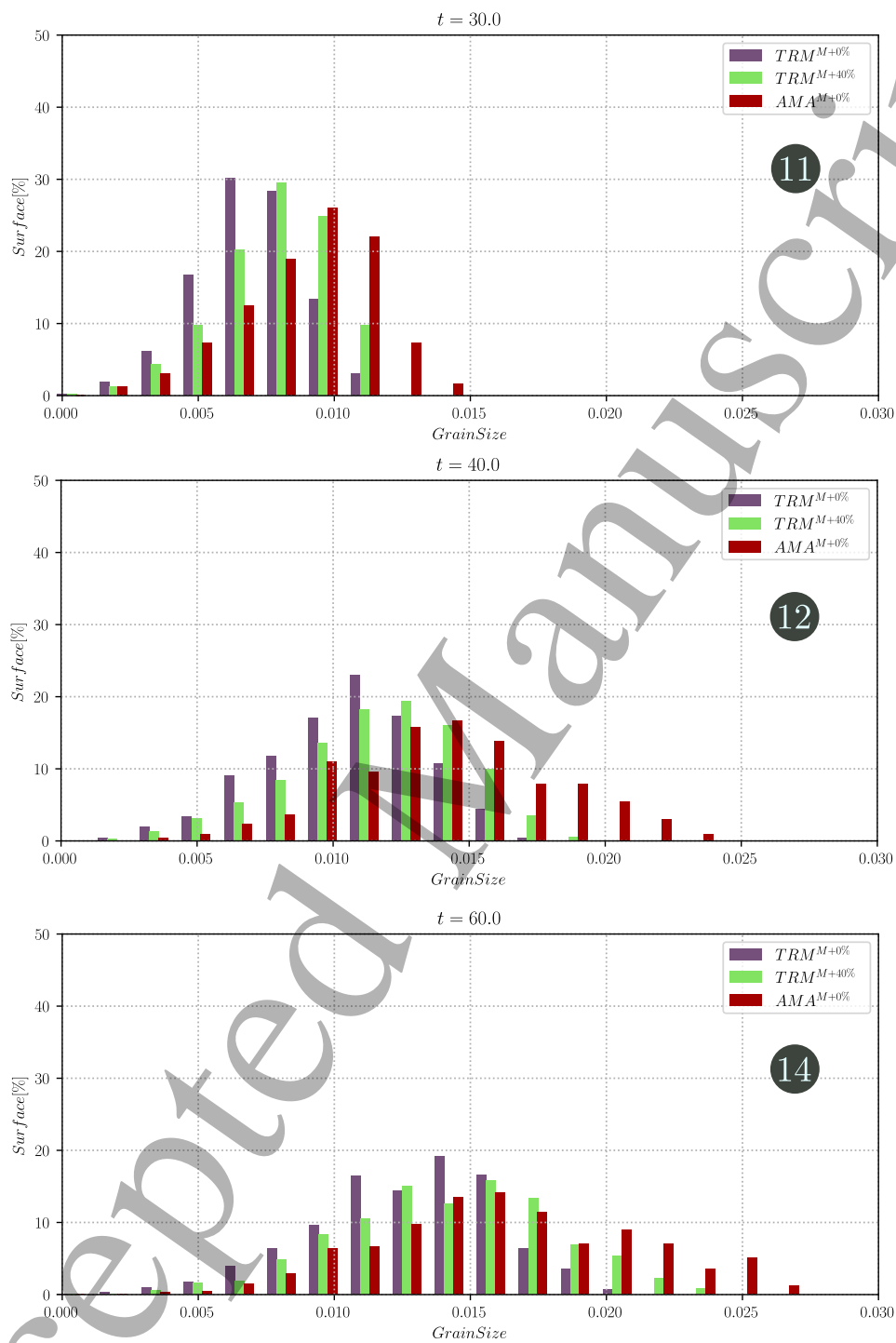


Figure 24: Grain size distributions pondered in surface for the states 11, 13 and 14 (example of a grain coarsening stage). The values are distributed more evenly on the size range (x axis) as a product of the grain growth.

A new front-tracking Lagrangian model for the modeling of DRX and PDRX 35

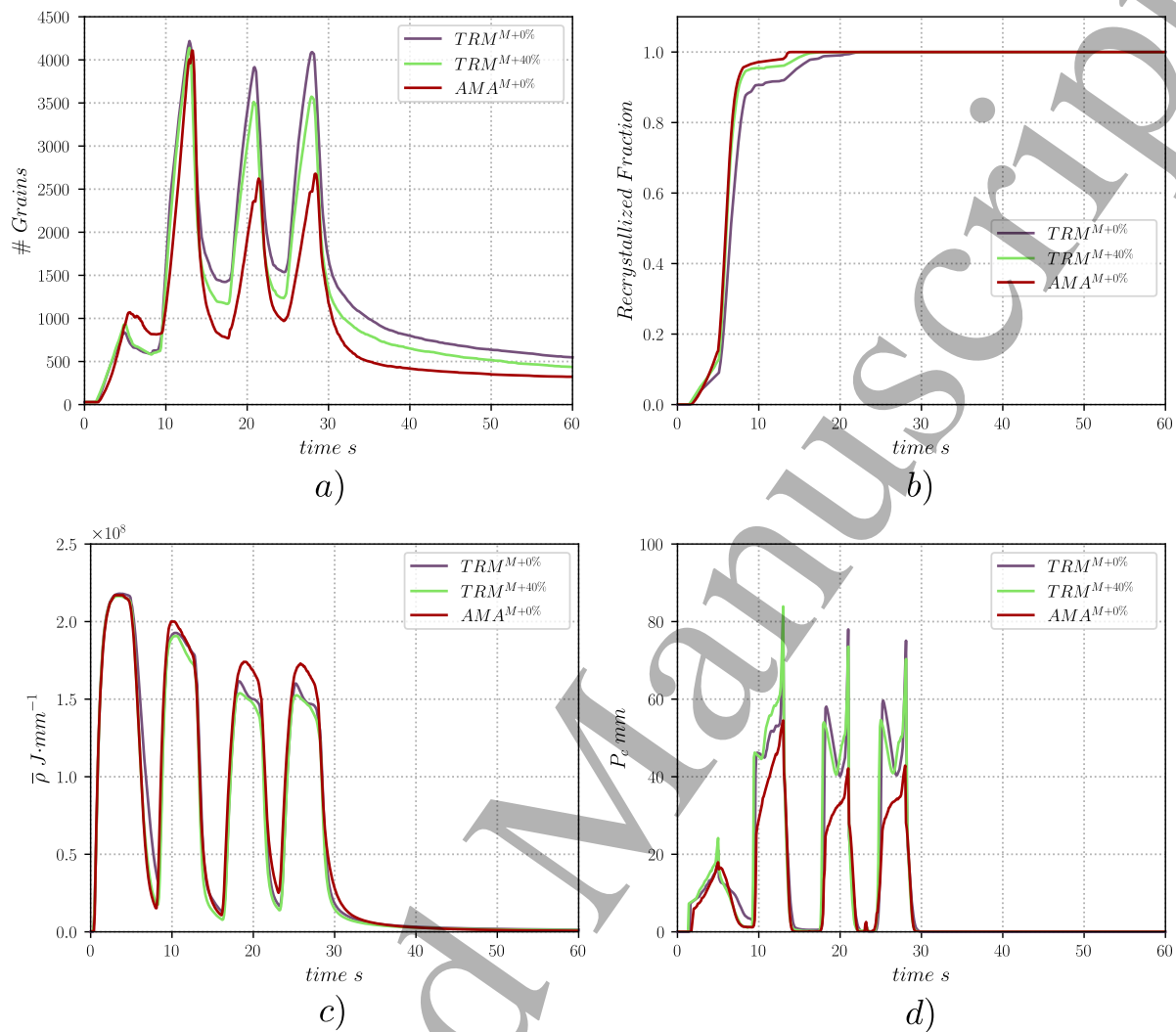


Figure 25: different values as a function of time for the DRX and PDRX test case, a) Number of grains, b) Recrystallized fraction, c) Mean value of ρ pondered by surface, and d) Critical perimeter for the computation of the nucleation rate in equation 13

A new front-tracking Lagrangian model for the modeling of DRX and PDRX 36

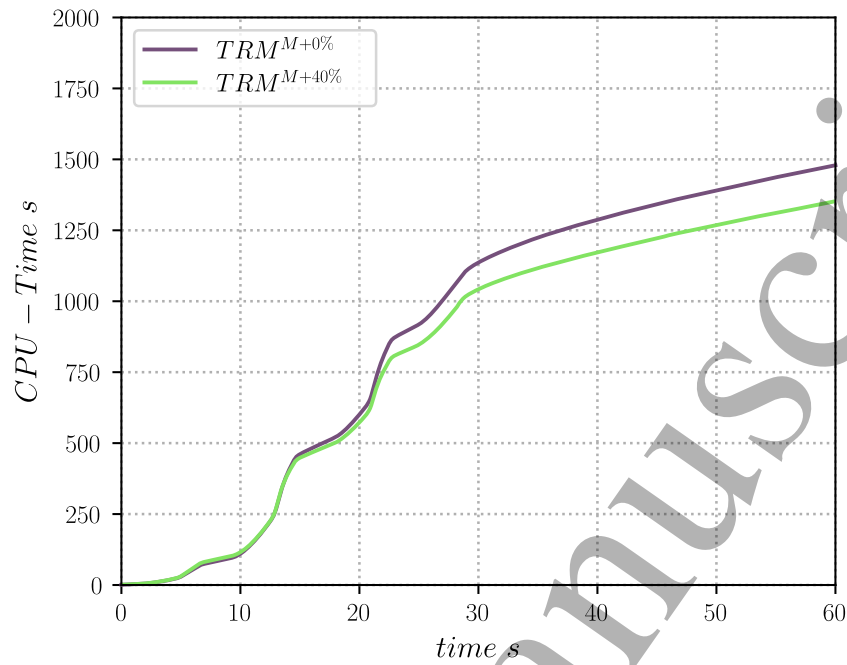


Figure 26: CPU-time for the different simulations using the TRM model, the computational cost drops as the number of simulated grains decreases.

6. Discussion, conclusion and perspectives

In this article the TRM model presented in previous works in the context of GBM by capillarity has been adapted in order to take into account bulk terms due to the SE during plastic deformation. This adaptation has made possible the integration of a recrystallization model to the TRM approach, for which a nucleation procedure has also been presented.

The algorithms presented in section 3.1 and represented by Eq. 6 for the computation of the velocity at multiple junctions, although intuitive have not been published before to the knowledge of the authors, only [37] shows a similar (more indirect) approach in the context of vertex simulations.

Results for the circle test case and tripe junction case have demonstrated the high accuracy of the TRM model in the modeling of boundary migration due to capillarity and SE, where in the normal context (for typical grain boundaries and multiple junctions), an error no greater than 2% was found. Also, the circle test case showed the typical behavior of a nucleus when subjected to a wide range of SE around its metastable point and helped define the safety factor ω used in Eq. 14, defining the minimal radius to nucleate in the context of the TRM model.

Finally, a DRX/PDRX test case was considered in order to test the recrystallization model provided in section 4 for 304L stainless steel at 1100 °C. A reference test case using the same ReX model but with a FE-LS strategy was also considered (AMA case) [17, 18, 36, 60]. Following the findings in [22], an optimal reduced mobility was calibrated to perform the tests (40% higher than the mobility used in the AMA case context). Results show a very good agreement between the two models. Moreover the CPU-times of the TRM model were much lower being between 20 to 25 minutes against the 4 hours and 38 minutes needed for the AMA case for its completion.

Perspectives for the presented work and the TRM approach include the implementation of a model able to treat full anisotropic boundary properties, as well as the study of the in-grain gradients of SE. The 3D implementation of the TRM model will also be studied in future works.

Acknowledgments

The authors thank the ArcelorMittal, ASCOMETAL, AUBERT & DUVAL, CEA, FRAMATOME, SAFRAN, TIMET, Constellium and TRANSVALOR companies and the ANR for their financial support through the DIGIMU consortium and ANR industrial Chair (Grant No. ANR-16-CHIN-0001).

References

- [1] A. D. Rollett, D. J. Srolovitz, M. P. Anderson, Simulation and theory of abnormal grain growth-anisotropic grain boundary energies and mobilities, *Acta Metallurgica* 37 (4) (1989) 1227–1240. doi:10.1016/0001-6160(89)90117-X.
- [2] A. D. Rollett, D. Raabe, A hybrid model for mesoscopic simulation of recrystallization, *Computational Materials Science* 21 (1) (2001) 69–78. doi:10.1016/S0927-0256(00)00216-0.
- [3] D. Raabe, Cellular automata in materials science with particular reference to recrystallization simulation, *Annual Review of Materials Science* 32 (2002) 53–76. doi:10.1146/annurev.matsci.32.090601.152855.
- [4] L. Barrales Mora, G. Gottstein, L. Shvindlerman, Three-dimensional grain growth: Analytical approaches and computer simulations, *Acta Materialia* 56 (20) (2008) 5915–5926. doi:10.1016/j.actamat.2008.08.006.
URL <https://linkinghub.elsevier.com/retrieve/pii/S1359645408005661>
- [5] L. Rauch, L. Madej, P. Szytkowski, R. Golab, Development of the cellular automata framework dedicated for metallic materials microstructure evolution models, *Archives of Civil and Mechanical Engineering* 15 (1) (2015) 48–61. doi:10.1016/j.acme.2014.06.006.
URL <http://dx.doi.org/10.1016/j.acme.2014.06.006>
- [6] L. Madej, M. Sitko, A. Legwand, K. Perzynski, K. Michalik, Development and evaluation of data transfer protocols in the fully coupled random cellular automata finite element model of dynamic recrystallization, *Journal of Computational Science* 26 (2018) 66–77. doi:10.1016/j.jocs.2018.03.007.
URL <https://doi.org/10.1016/j.jocs.2018.03.007>
- [7] I. Steinbach, F. Pezzolla, B. Nestler, M. Seeßelberg, R. Prieler, G. J. Schmitz, J. L. Rezende, A phase field concept for multiphase systems, *Physica D: Nonlinear Phenomena* 94 (3) (1996) 135–147. doi:10.1016/0167-2789(95)00298-7.
- [8] N. Moelans, B. Blanpain, P. Wollants, Quantitative analysis of grain boundary properties in a generalized phase field model for grain growth in anisotropic systems, *Physical Review B - Condensed Matter and Materials Physics* 78 (2). doi:10.1103/PhysRevB.78.024113.
- [9] C. E. Krill, L. Q. Chen, Computer simulation of 3-D grain growth using a phase-field model, *Acta Materialia* 50 (12) (2002) 3057–3073. doi:10.1016/s1359-6454(02)00084-8.
- [10] H. K. Kim, S. G. Kim, W. Dong, I. Steinbach, B. J. Lee, Phase-field modeling for 3D grain growth based on a grain boundary energy database, *Modelling and Simulation in Materials Science and Engineering* 22 (3). doi:10.1088/0965-0393/22/3/034004.
- [11] K. Kawasaki, T. Nagai, K. Nakashima, Vertex models for two-dimensional grain growth, *Philosophical Magazine B* 60 (3) (1989) 399–421. doi:10.1080/13642818908205916.
URL <https://www.tandfonline.com/doi/full/10.1080/13642818908205916>
- [12] D. Weygand, Y. Bréchet, J. Lépinoux, A vertex dynamics simulation of grain growth in two dimensions, *Philosophical Magazine B* 78 (4) (1998) 329–352. doi:10.1080/13642819808206731.
URL <https://www.tandfonline.com/doi/full/10.1080/13642819808206731>
- [13] J. Lépinoux, D. Weygand, M. Verdier, Modeling grain growth and related phenomena with vertex dynamics, *Comptes Rendus Physique* 11 (3-4) (2010) 265–273. doi:10.1016/j.crhy.2010.07.015.
URL <https://linkinghub.elsevier.com/retrieve/pii/S1631070510000800>
- [14] L. A. Barrales Mora, 2D vertex modeling for the simulation of grain growth and related phenomena, *Mathematics and Computers in Simulation* 80 (7) (2010) 1411–1427. doi:10.1016/j.matcom.2009.08.005.
URL <http://dx.doi.org/10.1016/j.matcom.2009.08.005>
- [15] Y. Mellbin, H. Hallberg, M. Ristinmaa, A combined crystal plasticity and graph-based vertex model of dynamic recrystallization at large deformations, *Modelling and Simulation in Materials Science and Engineering* 23 (4). doi:10.1088/0965-0393/23/4/045011.
- [16] B. Merriman, J. K. Bence, S. J. Osher, Motion of Multiple Junctions: A Level Set Approach,

A new front-tracking Lagrangian model for the modeling of DRX and PDRX 39

- Journal of Computational Physics 112 (2) (1994) 334–363. doi:10.1006/jcph.1994.1105.
- [17] M. Bernacki, Y. Chastel, T. Coupez, R. E. Logé, Level set framework for the numerical modelling of primary recrystallization in polycrystalline materials, *Scripta Materialia* 58 (12) (2008) 1129–1132. doi:10.1016/j.scriptamat.2008.02.016.
- [18] A. L. Cruz-Fabiano, R. Logé, M. Bernacki, Assessment of simplified 2D grain growth models from numerical experiments based on a level set framework, *Computational Materials Science* 92 (2014) 305–312. doi:10.1016/j.commatsci.2014.05.060.
- [19] L. Maire, B. Scholtes, C. Moussa, D. Pino Muñoz, N. Bozzolo, M. Bernacki, Improvement of 3-D mean field models for pure grain growth based on full field simulations, *Journal of Materials Science* 51 (24) (2016) 10970–10981.
- [20] J. Humphreys, G. S. Rohrer, A. Rollett, *Recrystallization and Related Annealing Phenomena* (Third Edition), Elsevier, 2017. doi:10.1016/B978-0-08-098235-9.00004-5.
- [21] M. Bernacki, N. Bozzolo, P. De Micheli, B. Flipon, J. Fausty, L. Maire, S. Florez, Numerical Modeling of Recrystallization in a Level Set Finite Element Framework for Application to Industrial Processes, in: *Recrystallization: Types, Techniques and Applications*, Nova, 2019.
- [22] S. Florez, K. Alvarado, D. P. Muñoz, M. Bernacki, A novel highly efficient Lagrangian model for massively multidomain simulation applied to microstructural evolutions, *Computer Methods in Applied Mechanics and Engineering* 367 (2020) 113107. doi:10.1016/j.cma.2020.113107. URL <https://doi.org/10.1016/j.cma.2020.113107>
- [23] S. Florez, J. Fausty, K. Alvarado, B. Murgas, M. Bernacki, A novel highly efficient Lagrangian model for massively multidomain simulations: parallel context, arXiv preprint arXiv:2009.04424.
- [24] M. Shakoor, P.-O. Bouchard, M. Bernacki, An adaptive level-set method with enhanced volume conservation for simulations in multiphase domains, *International Journal for Numerical Methods in Engineering* 109 (4) (2017) 555–576. doi:10.1002/nme.5297.
- [25] S. Florez, M. Shakoor, T. Toulorge, M. Bernacki, A new finite element strategy to simulate microstructural evolutions, *Computational Materials Science* 172 (2020) 109335. doi:10.1016/J.COMMATSCI.2019.109335.
- [26] B. Scholtes, M. Shakoor, A. Settefrati, P.-O. Bouchard, N. Bozzolo, M. Bernacki, New finite element developments for the full field modeling of microstructural evolutions using the level-set method, *Computational Materials Science* 109 (2015) 388–398. doi:10.1016/j.commatsci.2015.07.042.
- [27] B. Scholtes, R. Boulais-Sinou, A. Settefrati, D. Pino Muñoz, I. Poitroult, A. Montouchet, N. Bozzolo, M. Bernacki, 3D level set modeling of static recrystallization considering stored energy fields, *Computational Materials Science* 122 (2016) 57–71. doi:10.1016/j.commatsci.2016.04.045.
- [28] G. Compère, J. F. Remacle, E. Marchandise, Transient mesh adaptivity with large rigid-body displacements, *Proceedings of the 17th International Meshing Roundtable, IMR 2008 (iMMC)* (2008) 213–230. doi:10.1007/978-3-540-87921-3-13.
- [29] G. Compère, J.-F. Remacle, J. Jansson, J. Hoffman, A mesh adaptation framework for dealing with large deforming meshes, *International Journal for Numerical Methods in Engineering* 82 (7) (2010) 843–867. arXiv:1010.1724, doi:10.1002/nme.2788.
- [30] D. W. Walker, *Standards for message-Passing in a Distributed Memory Environment*, Tech. rep., Center for Research on Parallel Computing (CRPC), Oak Ridge National Lab., TN (United States) (1992).
- [31] G. Karypis, V. Kumar, A fast and high quality multilevel scheme for partitioning irregular graphs, *SIAM Journal of Scientific Computing* 20 (1) (1998) 359–392. doi:10.1137/S1064827595287997.
- [32] H. Hallberg, Influence of anisotropic grain boundary properties on the evolution of grain boundary character distribution during grain growth - A 2D level set study, *Modelling and Simulation in Materials Science and Engineering* 22 (8). doi:10.1088/0965-0393/22/8/085005.
- [33] J. Furstoss, M. Bernacki, C. Ganino, C. Petit, D. Pino-Muñoz, 2D and 3D simulation of grain growth in olivine aggregates using a full field model based on the level set method, *Physics of the Earth and Planetary Interiors* 283 (2018) 98–109.

A new front-tracking Lagrangian model for the modeling of DRX and PDRX 40

- [34] M. Bernacki, H. Resk, T. Coupez, R. E. Logé, Finite element model of primary recrystallization in polycrystalline aggregates using a level set framework, *Modelling and Simulation in Materials Science and Engineering* 17 (6) (2009) 64006. doi:10.1088/0965-0393/17/6/064006.
- [35] M. Bernacki, R. E. Logé, T. Coupez, Level set framework for the finite-element modelling of recrystallization and grain growth in polycrystalline materials, *Scripta Materialia* 64 (6) (2011) 525–528. doi:10.1016/j.scriptamat.2010.11.032.
- [36] L. Maire, B. Scholtes, C. Moussa, N. Bozzolo, D. P. Muñoz, A. Settefrati, M. Bernacki, Modeling of dynamic and post-dynamic recrystallization by coupling a full field approach to phenomenological laws, *Materials and Design* 133 (2017) 498–519. doi:10.1016/j.matdes.2017.08.015. URL <http://dx.doi.org/10.1016/j.matdes.2017.08.015>
- [37] H. Hallberg, A modified level set approach to 2D modeling of dynamic recrystallization, *Modelling and Simulation in Materials Science and Engineering* 21 (8) (2013) 85012. doi:10.1088/0965-0393/21/8/085012.
- [38] D. Weygand, Y. Bréchet, J. Lépinoux, Zener pinning and grain growth: a two-dimensional vertex computer simulation, *Acta Materialia* 47 (3) (1999) 961–970. doi:10.1016/S1359-6454(98)00383-8. URL <https://linkinghub.elsevier.com/retrieve/pii/S1359645498003838>
- [39] G. Couturier, C. Maurice, R. Fortunier, Three-dimensional finite-element simulation of Zener pinning dynamics, *Philosophical Magazine* 83 (30) (2003) 3387–3405. doi:10.1080/1478643031000152771.
- [40] G. Couturier, C. Maurice, R. Fortunier, R. Doherty, J. H. Driver, Finite element simulations of 3D Zener pinning, in: *Materials Science Forum*, Vol. 467-470, 2004, pp. 1009–1018. doi:10.4028/www.scientific.net/msf.467-470.1009.
- [41] G. Couturier, R. Doherty, C. Maurice, R. Fortunier, 3D finite element simulation of the inhibition of normal grain growth by particles, *Acta Materialia* 53 (4) (2005) 977–989. doi:10.1016/j.actamat.2004.10.044.
- [42] A. Agnoli, M. Bernacki, R. Logé, J. M. Franchet, J. Laigo, N. Bozzolo, Selective Growth of Low Stored Energy Grains During δ Sub-solvus Annealing in the Inconel 718 Nickel-Based Superalloy, *Metallurgical and Materials Transactions A: Physical Metallurgy and Materials Science* 46 (9) (2015) 4405–4421. doi:10.1007/s11661-015-3035-9.
- [43] D. N. Ilin, N. Bozzolo, T. Toulorge, M. Bernacki, Full field modeling of recrystallization: Effect of intragranular strain gradients on grain boundary shape and kinetics, *Computational Materials Science* 150 (March) (2018) 149–161. doi:10.1016/j.commatsci.2018.03.063.
- [44] L. Maire, J. Fausty, M. Bernacki, N. Bozzolo, P. De Micheli, and C. Moussa, A new topological approach for the mean field modeling of dynamic recrystallization, *Materials and Design*, 146 (1) (2018) 194–207. doi:10.1016/j.matdes.2018.03.011.
- [45] A. Laasraoui, J. J. Jonas, Prediction of steel flow stresses at high temperatures and strain rates, *Metallurgical Transactions A* 22 (7) (1991) 1545–1558. doi:10.1007/BF02667368.
- [46] A. L. Cruz-Fabiano, Modelling of crystal plasticity and grain boundary migration of 304L steel at the mesoscopic scale, Ph.D. thesis, MINES ParisTech (2014).
- [47] P. Peczak, M. J. Luton, The effect of nucleation models on dynamic recrystallization i. homogeneous stored energy distribution, *Philosophical Magazine B* 68 (1) (1993) 115–144. arXiv:<https://doi.org/10.1080/13642819308215285>, doi:10.1080/13642819308215285. URL <https://doi.org/10.1080/13642819308215285>
- [48] J. Bailey, P. B. Hirsch, The recrystallization process in some polycrystalline metals, *Proceedings of the Royal Society of London. Series A. Mathematical and Physical Sciences* 267 (1328) (1962) 11–30.
- [49] B. Scholtes, Development of an efficient level set framework for the full field modeling of recrystallization in 3D., Ph.D. thesis, MINES ParisTech (2016). arXiv:1410.7235, doi:10.1017/jfm.2015.566.
- [50] H. W. Hesselbarth, I. R. Göbel, Simulation of recrystallization by cellular automata, *Acta*

1
2
3 *A new front-tracking Lagrangian model for the modeling of DRX and PDRX* 41

- 4 Metallurgica Et Materialia 39 (9) (1991) 2135–2143. doi:10.1016/0956-7151(91)90183-2.
- 5 [51] C. H. Davies, Growth of nuclei in a cellular automaton simulation of recrystallisation, Scripta
6 Materialia 36 (1) (1997) 35–40. doi:10.1016/S1359-6462(96)00331-4.
- 7 [52] L. Sieradzki, L. Madej, A perceptive comparison of the cellular automata and Monte Carlo
8 techniques in application to static recrystallization modeling in polycrystalline materials,
9 Computational Materials Science 67 (2013) 156–173. doi:10.1016/j.commatsci.2012.08.047.
10 URL <http://dx.doi.org/10.1016/j.commatsci.2012.08.047>
- 11 [53] F. Villaret, B. Hary, Y. de Carlan, T. Baudin, R. Logé, L. Maire, M. Bernacki, Probabilistic and
12 deterministic full field approaches to simulate recrystallization in ODS steels, Computational
13 Materials Science 179 (March) (2020) 109646. doi:10.1016/j.commatsci.2020.109646.
14 URL <https://doi.org/10.1016/j.commatsci.2020.109646>
- 15 [54] F. Reitich, H. M. Soner, Three-phase boundary motions under constant velocities. I: The vanishing
16 surface tension limit, Royal Society of Edinburgh - Proceedings A 126 (4) (1996) 837–865.
17 doi:10.1017/S0308210500023106.
- 18 [55] J. E. Taylor, The motion of multiple-phase junctions under prescribed phase-boundary velocities,
19 Journal of Differential Equations 119 (1) (1995) 109–136. doi:10.1006/jdeq.1995.1085.
- 20 [56] H. Imai, M. Iri, K. Murota, Voronoi diagram in the Laguerre geometry and its applications, SIAM
21 Journal on Computing 14 (1) (1985) 93–105.
- 22 [57] K. Hitti, P. Laure, T. Coupez, L. Silva, M. Bernacki, Precise generation of complex statistical
23 Representative Volume Elements (RVEs) in a finite element context, Computational Materials
24 Science 61 (2012) 224–238. doi:10.1016/j.commatsci.2012.04.011.
- 25 [58] D. N. Ilin, M. Bernacki, Advancing layer algorithm of dense ellipse packing for generating statis-
26 tically equivalent polygonal structures, Granular Matter 18 (3) (2016) 43. doi:10.1007/s10035-
27 016-0646-9.
- 28 [59] L. Maire, Full field and mean field modeling of dynamic and post-dynamic recrystallization in 3D
29 – Application to 304L steel, Ph.D. thesis, PSL, Mines-ParisTech (2019).
- 30 [60] R. Logé, M. Bernacki, H. Resk, L. Delannay, H. Dignonnet, Y. Chastel, T. Coupez, Linking plastic
31 deformation to recrystallization in metals using digital microstructures, Philosophical Magazine
32 88 (30-32) (2008) 3691–3712. doi:10.1080/14786430802502575.
- 33
34
35
36
37
38
39
40
41
42
43
44
45
46
47
48
49
50
51
52
53
54
55
56
57
58
59
60